



SEDTRANS96: the upgraded and better calibrated sediment-transport model for continental shelves[☆]

Michael Z. Li*, Carl L. Amos

Geological Survey of Canada, Bedford Institute of Oceanography, Box 1006, Dartmouth, NS, B2Y 4A2 Canada

Received 30 November 1998; received in revised form 6 October 1999; accepted 6 October 1999

Abstract

The sediment transport model SEDTRANS has been significantly upgraded based on new advances in both cohesive and non-cohesive sediment transport studies. For given input data of wave, current, and seabed conditions, the model applies the combined wave–current bottom boundary layer theories to derive the near-bed velocity profile and bed shear stresses, and then calculates sediment transport for currents only or combined waves and currents over either cohesive or non-cohesive sediments. Critical shear stresses for various sediment transport modes tested for combined waves and currents are adopted in SEDTRANS96. An explicit combined-flow ripple predictor is included in the model to provide time-dependent bed roughness prediction. SEDTRANS96 also predicts the vertical profiles of velocity and suspended sediment concentration and their product is integrated through depth to derive the suspended-load transport rate. More rigorous calibration of the model using measured sediment transport rates over fine and medium sands shows that the difference between the predicted and measured transport rates has been reduced from more than one order of magnitude to less than a factor of five. The proposed new cohesive sediment algorithm separates cohesive sediment transport into depositional, stable and erosional states. The applied shear stress, erosion/deposition time duration and the down-core profile of the critical shear stress for erosion are numerically integrated to predict the final erosion or deposition rate, suspension concentration and transport rate for cohesive sediment. © 2001 Elsevier Science Ltd. All rights reserved.

Keywords: Current or combined wave–current flows; Cohesive or non-cohesive sediment transport; Computer simulation; Model prediction and field data

1. Introduction

The processes of sediment erosion, transport and deposition essentially occur in the bottom boundary layer which forms the interface between the seabed and the water column. These processes greatly affect seabed stability, the dispersal of particulate material and benthic communities. The study of bottom boundary

layer dynamics and sediment transport is thus important to oceanographers, coastal engineers as well as environmental managers (Grant and Madsen, 1986; Wright, 1989; Cacchione and Drake, 1990). SEDTRANS is a one-dimensional numerical computer model developed at the Geological Survey of Canada — Atlantic (GSCA) to deal with the boundary layer dynamics and sediment transport problems on continental shelves and in coastal environments (Martec Ltd., 1984, 1987; Davidson and Amos, 1985). Several other 1-D sediment transport models have also been developed (e.g. Smith, 1977; Wiberg et al., 1994; Grant and Madsen, 1979; Glenn and Grant, 1987). These are more basic bottom boundary layer models with a focus on suspension prediction over

[☆]Code available from server at <http://www.iamg.org/CGEditor/index/htm>.

*Corresponding author. Tel.: 1-902-426-9459; fax: 1-902-426-4104.

E-mail address: li@agc.bio.ns.ca (M.Z. Li).

Nomenclature

A	empirical coefficient for downcore sediment resistance
A_b	near-bed wave orbital amplitude (L)
c	sediment concentration (M L^{-3})
C_b	volume concentration of the bottom sediment
$C_{\delta\text{cw}}$	suspended sediment concentration at the height of the wave–current boundary layer (M L^{-3})
C_{dir}	direction of mean current
C_r	wave-to-current strength ratio
c_t	time-dependent suspended sediment concentration (M L^{-3})
C_z	suspended sediment concentration at height z above the seabed (M L^{-3})
c_0	initial suspended sediment concentration (M L^{-3})
C_0	reference suspended sediment concentration at the height of bed roughness z_0 (M L^{-3})
D	(median) sediment grain diameter (L)
E_m	eroded mass (M)
E_0	empirical coefficient for minimum erosion
F	fraction of the size class in bottom sediment
f_c, f_{cs}	current friction factor
$f_{\text{cw}}, f_{\text{cws}}$	combined wave–current friction factor
f_w, f_{ws}	wave friction factor
g	acceleration due to gravity (M T^{-2})
h	water depth (L)
H_b	height of breaking waves (L)
H_s	significant wave height (L)
h_{tm}	thickness scale of the bedload layer (L)
I	option number of transport equation
k	wave number
K	proportionality coefficient in Bagnold transport formula
k_b	total bed roughness height (L)
k_{bg}	sediment grain roughness height (L)
k_{br}	ripple roughness height (L)
k_{bt}	bedload-transport roughness height (L)
$(L_0) L$	(deep-water) wavelength (L)
m	sediment mass (M)
M	empirical coefficient in Bagnold transport formula
P_e	proportionality coefficient for erosion
P_s	probability coefficient of resuspension
q	volume rate of sediment transport ($\text{L}^2 \text{T}^{-1}$)
Q_b	mass bedload transport rate ($\text{M T}^{-1} \text{L}^{-1}$)
$Q_{b\text{--dir}}$	direction of bedload transport
Q_m	mass bedform transport rate ($\text{M T}^{-1} \text{L}^{-1}$)
$(Q_{s0}) Q_s$	(initial) suspended-load transport rate ($\text{M T}^{-1} \text{L}^{-1}$)
r_d	deposition rate of cohesive sediments ($\text{M T}^{-1} \text{L}^{-2}$)
r_e	erosion rate of cohesive sediments ($\text{M T}^{-1} \text{L}^{-2}$)
R_m	ripple migration rate (L T^{-1})
S_*	dimensionless sediment parameter
$t, \Delta t$	time and time interval (T)
T	wave period (T)
t_b	time of bedload transport over a 1/2 wave cycle (T)
t_s	time of suspended-load transport over a 1/2 wave cycle (T)
u	mean current velocity (L T^{-1})
u_b	near-bed maximum wave orbital velocity (L T^{-1})
u_{cr}	critical mean velocity (L T^{-1})
u_z	mean velocity at height z above the bottom (L T^{-1})
u_{100}	mean velocity at 1 m above the bottom (L T^{-1})

u_*	shear velocity ($L T^{-1}$)
u_{*bf}	critical shear velocity for ripple break-off ($L T^{-1}$)
u_{*c}, u_{*cb}, u_{*cs}	total/bedload/skin-friction current shear velocity ($L T^{-1}$)
u_{*cr}	critical shear velocity for bedload transport ($L T^{-1}$)
u_{*crs}	critical shear velocity for suspended-load transport ($L T^{-1}$)
$u_{*cw}, u_{*cwb}, u_{*cws}$	total/bedload/skin-friction combined wave-current shear velocity ($L T^{-1}$)
u_{*cwe}	ripple-enhanced combined shear velocity ($L T^{-1}$)
u_{*up}	critical shear velocity for upper-plane bed sheet-flow ($L T^{-1}$)
u_{*w}, u_{*wb}, u_{*ws}	total/bedload/skin-friction wave shear velocity ($L T^{-1}$)
W_{dir}	wave propagation direction
W_s	particle settling velocity ($L T^{-1}$)
W_{sc}	settling velocity for cohesive sediment ($L T^{-1}$)
Y	Yalin parameter
z	height above the bottom (L)
z_r	height of measured mean current (L)
z_s	downcore sediment depth (L)
z_0	bottom roughness (L)
z_{0c}	apparent bottom roughness (L)

Greek letters

$\alpha, \alpha_1, \alpha_2$	Rouse suspension parameter
β	bed slope or grain size coefficient in the modified Bagnold formula
γ_0	empirical sediment resuspension coefficient
δ_{cw}	thickness of wave-current boundary layer (L)
$(\eta_p) \eta$	(pre-existing) ripple height (L)
θ_{cr}	Shields parameter for bedload transport
θ_{cs}	skin-friction current Shields parameter
θ_{cws}	skin-friction combined Shields parameter
θ_{up}	Shields parameter for sheet-flow
θ_{ws}	skin-friction wave Shields parameter
κ	von Karman constant
$(\lambda_p) \lambda$	(pre-existing) ripple wavelength (L)
μ	dynamic fluid viscosity ($M T^{-1} L^{-1}$)
ν	kinematic fluid viscosity ($L^2 T^{-1}$)
ρ	fluid density ($M L^{-3}$)
ρ_b	sediment bulk density ($M L^{-3}$)
ρ_s	sediment density ($M L^{-3}$)
σ	ripple break-off index
τ_b	bottom shear stress ($M L T^{-2} L^{-2}$)
τ_{cr}	critical shear stress for bedload transport ($M L T^{-2} L^{-2}$)
τ_{crs}	critical shear stress for suspended-load transport ($M L T^{-2} L^{-2}$)
τ_{cs}	skin-friction current shear stress ($M L T^{-2} L^{-2}$)
τ_{cwe}	ripple-enhanced combined shear stress ($M L T^{-2} L^{-2}$)
τ_{cws}	skin-friction combined shear stress ($M L T^{-2} L^{-2}$)
$\tau_{cws}(t)$	instantaneous skin-friction combined shear stress ($M L T^{-2} L^{-2}$)
τ'_{cws}	effective bed shear stress ($M L T^{-2} L^{-2}$)
τ_d	critical deposition shear stress for cohesive sediments ($M L T^{-2} L^{-2}$)
τ_e	critical erosion shear stress for cohesive sediments ($M L T^{-2} L^{-2}$)
$\tau_e(z)$	critical erosion shear stress as a function of sediment depth ($M L T^{-2} L^{-2}$)
$\tau_e(0)$	critical erosion shear stress at the sediment surface ($M L T^{-2} L^{-2}$)
τ_{up}	critical shear stress for sheet-flow ($M L T^{-2} L^{-2}$)
τ_w, τ_{ws}	total/skin-friction wave shear stress ($M L T^{-2} L^{-2}$)
τ_y	yield stress for cohesive sediments ($M L T^{-2} L^{-2}$)

τ_*	normalized excess shear stress
ϕ_b	angle between wave and current in the wave–current boundary layer
ϕ_i	internal friction angle for cohesive sediment
ω	wave angular frequency (T^{-1})

sand sediment, while SEDTRANS is a more comprehensive model which not only gives boundary layer parameters but also predicts bedform development, bedload as well as suspended load transport rates for both sand and cohesive sediments. Also calculations under pure wave, pure current and combined wave–current conditions are treated in separate algorithms. The original model was re-evaluated and upgraded by Li and Amos (1995) based on advances in combined-flow bottom boundary layer theory (Grant and Madsen, 1986) and limited field measurements of sediment transport (Amos et al., 1988). The upgraded version of the model, SEDTRANS92, has been successfully applied to predicting sediment transport on the Scotian Shelf (Anderson, 1995; Li et al., 1997).

As stated in Li and Amos (1995), SEDTRANS92 has several shortcomings. The model does not have a time-dependent bed roughness predictor. So when bedform measurements are not available, the model uses a mean ripple height, provided by the user, to compute friction factor and bed shear stresses. This approach has neglected the interaction between the prevailing flow dynamics and the equilibrium bedforms. SEDTRANS92 does predict bedform dimension for some grain sizes, but only for output purposes. Due to the lack of ripple predictors for combined waves and currents, mixed wave ripple and current ripple predictors have to be used in the model. SEDTRANS92 is also only calibrated (with limited data) for bedload transport and it does not include a separate algorithm for the prediction of suspended load transport which is more important during storms or for fine-grained sediment.

Several recent studies have advanced our understanding of boundary layer dynamics, the development of bedforms, and their effects on shear stress partition and sand resuspension (e.g. Wiberg and Nelson, 1992; Wright, 1993; Madsen et al., 1993; van Rijn et al., 1993; Li, 1994; Vincent and Downing, 1994; Wiberg and Harris, 1994; Wright et al., 1994; van Rijn and Havinga, 1995; Li et al., 1996). Field projects conducted by GSCA on the Scotian Shelf also led to several key advances: the establishment of threshold shear stresses for various transport modes under combined waves and currents, a new empirical ripple predictor explicitly for combined-flow conditions, and

more field data for fuller calibration of sediment transport models (Li et al., 1997; Li and Amos, 1998, 1999b). Due to the development of new field instruments (Amos et al., 1992a; Maa et al., 1993), significant advances have also been made in our understanding of cohesive sediment transport, particularly in in situ measurements of cohesive sediment stability, temporal and spatial changes of cohesive sediment erodibility, and the correlation between the erodibility and physical/biological properties of sediment (Mehta, 1993; Amos et al., 1996, 1997).

Based on these significant advances in both cohesive and non-cohesive sediment transport studies, a major upgrade has been performed on SEDTRANS92 (Li and Amos, 1997). The objective of this paper is to describe the newly upgraded and calibrated GSC sediment transport model, SEDTRANS96. The key improvements in SEDTRANS96 include (1) tested critical shear stresses for various transport modes under combined flows, (2) new ripple predictor for combined waves and currents and hence time-dependent prediction of bed roughness, (3) predictions of suspended load transport added, (4) upgraded algorithms for cohesive sediment transport, and (5) more rigorous calibration of the model with new field data. The model structure and operation is first described. Following this are the discussions of the theories of the main subroutines of the model. Finally, new field data is used to carry out more comprehensive calibration of the model. The sample runs of the model are given in Appendices A and B at the end of the paper and a list of the symbols used is given in nomenclature.

2. Model structure and operation

SEDTRANS96 is a one-dimensional computer model that can be used to predict the transport rate and direction of sand or mud under either steady currents or combined waves and currents outside the breaking zone. SEDTRANS96 adopts the Grant and Madsen (1986) continental shelf bottom boundary layer theory (GM86 hereafter) to predict bed shear stresses and the velocity profile in the bottom boundary layer. The model uses the algorithms of Einstein-Brown (Brown, 1950) and Yalin (1963) for bedload prediction. The methods of

Engelund and Hansen (1967) and Bagnold (1963) are used to determine total load transport (bedload plus suspended load). At the present, SEDTRANS96 uses the median grain size of bottom sediment in its calculations and does not deal with the effect of grain size distribution. The prediction of cohesive sediment transport adopts a new algorithm proposed by Li and Amos (1997) based on Amos and Greenberg (1980) and Amos et al. (1996, 1997).

SEDTRANS96 is written in standard Fortran77. It can be run either interactively or in batch mode. The source code of the model is made modular to simplify the computational processes and allow each subroutine to be modified separately without having to change the whole program. There are 11 subroutines in the model. These subroutines and their main functions are given below:

1. Main programs, IAFSED (interactive mode) and BCHSED (batch mode): control passage of information among subroutines.
2. Subroutines READIN (interactive mode) and READBCH (batch mode): read user-supplied data required to run the model.
3. Subroutine INOUT: prints the input data both to the terminal and to the output files.
4. Subroutine OSCIL: computes the required wave parameters using linear wave theory.
5. Subroutine THRESH: calculates the threshold shear stresses and shear velocities for various sediment transport modes.
6. Subroutine FRICFAC: calculates the friction factor, bedform geometry and various shear stresses required by the program.
7. Subroutine TIMING: calculates the duration of bedload and suspended load transport during a wave cycle.
8. Subroutine TRANSP: computes the time-averaged net sediment transport according to one of five available algorithms.
9. Subroutine PROF: predicts the profiles of mean velocity and suspended sediment concentration and integrates them to derive the suspended load transport rate and direction.
10. Subroutine BEDFORM: predicts the possible types of bedforms.
11. Subroutine OUTOUT: prints the selected output parameters from all the subroutines both to the terminal and to the output files.

The following input data of wave, current and seabed parameters are required to run SEDTRANS96: water depth h (m), mean current velocity u (m s^{-1}) and its direction C_{dir} (deg), height of current measurement above the sea bed z_r (m), significant wave height H_s (m),

wave period T (s), wave propagation direction W_{dir} (deg), median sediment grain size D (m), ripple height η (m), ripple wavelength λ (m), and bed slope β (deg). For a given set of wave, current and seabed conditions, the subroutine OSCIL is first run to calculate related wave parameters based on the linear wave theory. Subroutine THRESH is then used to determine the critical shear stresses for bedload, suspended load and upper-plane bed sheet-flow sediment transport, respectively. Friction factors, bed shear stresses and bedform geometry are predicted in subroutine FRICFAC. Based on the results from OSCIL, THRESH and FRICFAC, the duration of bedload and suspended load sediment transport over a wave cycle are calculated in subroutine TIMING and net sediment transport rates are obtained in subroutine TRANSP by integration of the instantaneous sediment transport rate through a wave cycle. Subroutine PROF is then run (for non-cohesive sediment only) to predict the profiles of velocity and suspended sediment concentration which are vertically integrated to obtain the rate of suspended load sediment transport. Based on near-bed velocities and shear stresses, bedform types are predicted in BEDFORM and finally subroutine OUTOUT outputs results to the monitor and data files. The key output parameters from SEDTRANS96 include near-bed maximum wave orbital velocity u_b (m/s), wave excursion amplitude A_b (m), predicted bedform types and dimension (ripple height and wavelength), various wave and current shear velocities, and the magnitude and direction of bedload and suspended load sediment transport.

In this latest version of SEDTRANS, several batch files are used to control the model running and result output. By typing **menu96** and pressing Enter, a menu is displayed and the user can choose to run the model in interactive or batch mode (Appendix A). For the interactive mode, SEDTRANS96 is started by running the executable file IAFSED. The model will prompt for each of the input parameters. The detailed output text is stored in a file specified by the user and the parameters are stored in two tabular files SEDOUT1 and SEDOUT2. The predicted velocity and suspended sediment concentration profiles are saved in PROFILE.DAT. An example of an interactive session of SEDTRANS96 and its output files are given in Appendix A. For the batch mode SEDTRANS96, the model is run by executing the file BCHSED. The input data INDATA need to be prepared in advance and is called by BCHSED in batch mode runs. Detailed text outputs are saved in OUTDATA and the output parameters are saved to SEDOUT1.DAT and SEDOUT2.DAT in tabular format. The predicted velocity and suspended sediment concentration profiles are stored in a file named PROFILE. Examples of INDATA, SEDOUT1.DAT, SEDOUT2.DAT and PROFILE files for running the batch-mode

SEDTRANS96 can be found in Appendix B. When the model is completed, it returns to the main menu and the user can choose to run the model again with new data or terminate the model and go back to DOS.

3. Theories of main subroutines

The computations of SEDTRANS96 mainly occur in seven subroutines. These subroutines are: OSCIL, FRICFAC, THRESH, TIMING, TRANSPO, PROFL and BEDFORM. The theories and algorithms behind these subroutines have been described in Li and Amos (1995). Only the key equations and enhancements in SEDTRANS96 are given next:

3.1. Subroutine OSCIL

Subroutine OSCIL employs the linear wave theory to calculate the maximum wave orbital velocity (u_b) and maximum wave orbital excursion amplitude (A_b), which are needed in the calculation of wave and combined-flow bed shear stresses. The required input parameters for this subroutine are significant wave height (H_s), wave period (T), and water depth (h).

Wave number k is computed from the linear wave dispersion equation

$$\omega^2 = gk \tanh(kh), \quad (1)$$

where ω is the wave angular frequency ($\omega = 2\pi/T$), g is the acceleration due to gravity and \tanh is the hyperbolic tangent function. The wave number so obtained is then used in the following equation to determine wavelength L :

$$L = L_o \tanh(kh), \quad (2)$$

where $L_o = gT^2/2\pi$ is the deep-water wavelength. For non-breaking waves, the required wave parameters u_b and A_b are calculated from

$$u_b = \pi H/[T \sinh(kh)], \quad (3)$$

$$A_b = u_b/\omega, \quad (4)$$

where \sinh is the hyperbolic sine. The condition of breaking waves is given by Miche (1944) as $H_b = 0.142L \tanh(kh)$, where H_b is the height of breaking waves. The program will be terminated when this situation occurs. It should be noted that the extension of linear wave theory up to breaking waves could cause errors due to ignoring the effects of asymmetrical wave oscillation.

3.2. Subroutine THRESH

As bed shear stress increases, sediment particles will first be entrained from their resting positions and then go through three distinctive modes of transport, i.e. bedload, suspension and sheet-flow transport. Accurate predictions of sediment transport rates very much depend on the establishment of the critical shear stresses for the initiation of these three transport modes. Subroutine THRESH calculates, respectively, the critical shear velocities for these transport modes based on the latest data we collected from Scotian Shelf. Since seabed scouring and intensive sediment transport mostly occur under upper-plane bed sheet-flow, the main enhancement from SEDTRANS92 is the addition of the computation of the critical shear stress for sheet-flow transport. All transport algorithms in SEDTRANS use the modified Shields curve to determine the threshold of bedload transport, except the total-load method of Ackers and White (1973) which uses a complex threshold criterion. Thus Ackers and White (1973) method is not included in SEDTRANS96.

As in SEDTRANS92, the critical shear velocity for bedload transport, u_{*cr} , was adopted as the threshold criterion in SEDTRANS96. The Yalin's method according to Miller et al. (1977) has been used to obtain the dimensionless critical Shields parameter θ_{cr} :

$$\log \theta_{cr} = 0.041(\log Y)^2 - 0.356 \log Y - 0.977, \quad Y < 100, \quad (5a)$$

$$\log \theta_{cr} = 0.132 \log Y - 1.804, \quad 100 < Y \leq 3000, \quad (5b)$$

$$\theta_{cr} = 0.045, \quad Y > 3000, \quad (5c)$$

where the Yalin parameter Y is defined as $[(\rho_s - \rho)gD^3/\rho\nu^2]^{0.5}$, ρ_s and ρ are, respectively, sediment and fluid densities. This θ_{cr} value can be used in turn to calculate the critical shear stress τ_{cr} from:

$$\tau_{cr} = \theta_{cr}(\rho_s - \rho)gD \quad (6)$$

and the critical shear velocity u_{*cr} is obtained from the quadratic law $\tau_{cr} = \rho u_{*cr}^2$.

To compute the critical shear velocity for suspension transport, the settling velocity W_s of a sediment grain of diameter D is first calculated from Gibbs et al. (1971):

$$W_s = \{-3\mu + [9\mu^2 + (gD^2/4)\rho(\rho_s - \rho)(0.0155 + 0.0992D)]^{0.5}/[\rho(0.0116 + 0.0744D)]\}, \quad (7)$$

where μ is the dynamic viscosity. The critical shear stress for the initiation of suspended load transport, τ_{crs} , is then computed from Bagnold (1966)

$$\tau_{crs} = 0.64\rho W_s^2 \quad (8)$$

or converted to the critical shear velocity u_{*crs} :

$$u_{*crs} = 0.8W_s. \quad (9)$$

Various criteria have been suggested for sheet flow under waves, but no consensus has been reached (e.g. Manohar, 1955; Komar and Miller, 1975; Dingler and Inman, 1976). Data of sheet flow under combined waves and currents are very limited (see Hay and Bowen, 1993; Madsen et al., 1993; Dick et al., 1994). Li and Amos (1999a) have compiled data from previous studies and compared them to their field observations on the Scotian Shelf in attempting to derive a universal criterion. SEDTRANS96 adopts their findings to predict the critical Shields parameter for sheet-flow as

$$\theta_{up} = 0.172D^{-0.376}, \quad (10)$$

where particle size D is in cm. The corresponding critical shear stress for sheet flow is obtained from:

$$\tau_{up} = \rho u_{*up}^2 = \theta_{up}(\rho_s - \rho)gD \quad (11)$$

in which u_{*up} is the critical shear velocity for sheet flow.

Recent hydrodynamics and sediment transport studies, however, have shown that enhanced shear stresses due to ripples and bedload transport have to be compared against these threshold criteria in order to properly predict the onset and durations of various transport modes under combined waves and currents (Li et al., 1997; Li and Amos, 1999b). Similar findings can also be found in Kapdasli and Dyer (1986), Wilson (1988), Wiberg and Nelson (1992) and Wiberg and Harris (1994). These effects are further discussed in the sections on subroutine FRICFAC and model calibration.

3.3. Subroutine FRICFAC

Friction factors, bedform geometry and various bed shear stresses are predicted in subroutine FRICFAC. One of the modifications made in SEDTRANS96 is that the height and length of bedforms are now predicted in subroutine FRICFAC instead of in subroutine BEDFORM so that a time-dependent bed roughness and its effects on boundary layer parameters are included. The types of bedforms, however, are still predicted in subroutine BEDFORM. In addition, the GM86 model assumes that the total bed roughness is composed of grain roughness, bedform (ripple) roughness as well as bedload roughness when sediment is in transport. The FRICFAC subroutine of SEDTRANS96 thus has been modified so that the sum of grain, bedform and bedload roughness heights now is used in the calculation of total friction factor and shear stresses for the combined-flow case. SEDTRANS92 included the method of Smith (1977) for predicting combined-flow friction factors under current-dominant conditions. However, several uncertain assumptions were made in using the Smith method, and the predicted friction factors and sediment transport rates were found to be incompatible

with those based on the Grant and Madsen method (Martec Ltd., 1987). A recent study by Xu et al. (1994) has also shown that the Grant and Madsen (1986) method could also be applied to a current-dominant situation. For these reasons, the Smith (1977) method is no longer included.

3.3.1. Wave- or current-only cases

The computation of friction factor for either the pure wave or the steady current case is not changed in SEDTRANS96. The steady-current skin-friction factor f_{cs} is taken to be 0.006 based on field experiments of Sternberg (1972) and Soulsby (1983). Wave friction factor f_w is calculated according to Jonsson (1966) as modified by Nielsen (1979):

$$f_w = \exp[5.213(k_b/A_b)^{0.194} - 5.977], \quad (12a)$$

$$A_b/k_b > 1.7,$$

$$f_w = 0.28, \quad A_b/k_b \leq 1.7, \quad (12b)$$

where k_b is the bottom roughness height. A quadratic law is used to compute the bottom shear stress τ_b .

For pure waves:

$$\tau_b = 0.5\rho f_w u_b^2 \quad (13)$$

and for steady currents:

$$\tau_b = 0.5\rho f_c u_{100}^2, \quad (14)$$

where f_c is the current friction factor and u_{100} is the mean velocity at 1 m above the bottom.

For the wave-only case, the grain size roughness height of $2.5D$ is first used in place of k_b in Eq. (12) to calculate the skin-friction wave friction factor f_{ws} . This is used in Eq. (13) for the computation of skin-friction wave shear stress τ_{ws} . This stress is used in Eqs. (19) and (20) (see the following text) to predict the ripple height and wavelength. The predicted ripple dimensions are used in the following equation (Grant and Madsen, 1982) to obtain the ripple roughness height k_{br} :

$$k_{br} = 27.7\eta(\eta/\lambda). \quad (15)$$

This new roughness height is again used in Eqs. (12) and (13) to obtain the total wave friction factor f_w and total wave shear stress $\tau_w = \rho u_{*w}^2$, where u_{*w} is the total wave shear velocity. The bottom roughness length is calculated from $z_0 = k_{br}/30$.

For the current-only case, if input ripple height and wavelength are available, they will be used in Eq. (15) to obtain an initial estimate of the bed roughness height k_b . Otherwise, the initial bed roughness height will be the grain roughness height $2.5D$. This initial bed roughness height together with the measured mean velocity u_z at height z are used to estimate the total current shear velocity u_{*c} in the von Karman–Prandtl law-of-wall

equation

$$u_{*c} = \kappa u_z / \ln(30z/k_b), \quad (16)$$

where κ is the von Karman constant ($=0.4$). The initial estimate of the mean velocity at 1 m above the seabed is then obtained from

$$u_{100} = (u_{*c}/\kappa) \ln(30 \times 100/k_b), \quad (17)$$

where 100 in the natural log function is used assuming all other parameters are in cgs units. The mean velocity u_{100} and current skin-friction factor $f_{cs} = 0.006$ are then used in Eq. (14) to obtain the skin-friction current shear stress (or shear velocity u_{*cs}) $\tau_{cs} = \rho u_{*cs}^2$. This shear stress is then compared against τ_{cr} , τ_{up} , and used in Eqs. (18) and (20) (see the following text) to predict ripple geometry. If the predicted ripple height is zero (sheet-flow or $u_{*cs} < u_{*cr}$ and input ripple height is 0), the new bed roughness height is obtained from the von Karman–Prandtl law of wall $k_b = \exp[\ln(30z) - \kappa u_z / u_{*c}]$ (see Eq. (16)). Otherwise if the predicted ripple height is not zero, the new bed roughness height will be given by Eq. (15). With this new estimate of bed roughness height, the above procedures are repeated until the values of u_{*cs} converge. Finally the bottom roughness length is calculated from $z_0 = k_b/30$.

As field measurements of ripples are scarce for coarse and very coarse sands (e.g. Forbes and Boyd, 1987), bedform heights and lengths are not predicted for these grain sizes. Under either steady currents or pure waves, the skin-friction shear stress τ_b is compared with the critical shear stresses for bedload and sheet-flow transports, τ_{cr} and τ_{up} , respectively. If $\tau_b < \tau_{cr}$, sediment transport does not occur and the input values of bedform height and length will be used. If $\tau_b \geq \tau_{up}$, upper-plane bed sheet-flow occurs and ripples are completely washed out. Only when $\tau_{cr} \leq \tau_b < \tau_{up}$, will bedform dimensions be estimated. The ripple wavelength λ under steady currents is predicted according to Yalin (1964):

$$\lambda = 1000D \quad (18)$$

and that under waves is given according to Boyd et al. (1988):

$$\lambda = 557 A_b (u_b A_b / v)^{-0.68}. \quad (19)$$

The ripple height η under both conditions is predicted following Allen (1970):

$$\eta = 0.074 \lambda^{1.19} \quad (20)$$

in which λ needs to be in cm.

3.3.2. Combined-flow case

The calculation of the combined-flow friction factor f_{cw} and various shear stresses in SEDTRANS96 follows the GM86 model and is undertaken in three steps:

(1) *Initial estimate of f_{cw}* : An arbitrary value is first assumed for the relative strength ratio of wave to current C_r . The friction factor f_{cw} can then be obtained by iteration from

$$\begin{aligned} & 1/(4f_{cw}^{0.5}) + \log[1/(4f_{cw}^{0.5})] \\ & = \log(C_r u_b / \omega z_0) + 0.14(4f_{cw}^{0.5}) - 1.65, \end{aligned} \quad (21)$$

where $z_0 = k_b/30$ is the bottom roughness. To compute various bed shear stresses, different values of roughness height k_b have to be used in Eq. (21) (see the following text for explanation).

(2) *Estimating shear velocities u_{*c} , u_{*w} and u_{*cw}* : The maximum wave shear velocity u_{*w} is calculated using C_r and f_{cw} from above:

$$u_{*w} = (C_r f_{cw} u_b^2 / 2)^{0.5} \quad (22)$$

and the shear velocity due to combined waves and currents is obtained from

$$u_{*cw} = u_{*w} C_r^{0.5}. \quad (23)$$

The equations governing the near-bed velocity profiles in GM86 model are

$$u_z = (u_{*c}/\kappa)(u_{*c}/u_{*cw}) \ln(z/z_0), \quad z \leq \delta_{cw}, \quad (24a)$$

$$u_z = (u_{*c}/\kappa) \ln(z/z_{0c}), \quad z \geq \delta_{cw}, \quad (24b)$$

where u_{*c} is the total current shear velocity, z_{0c} is the apparent bed roughness experienced by the current in the presence of waves, and $\delta_{cw} = 2\kappa u_{*cw}/v$ is the thickness of the wave–current boundary layer. By matching the current of the outer layer ($z \geq \delta_{cw}$) and that of the wave boundary layer ($z \leq \delta_{cw}$) at the height of δ_{cw} , current shear velocity u_{*c} can be computed from the following:

$$u_z = (u_{*c}/\kappa)[(u_{*c}/u_{*cw}) \ln(\delta_{cw}/z_0) + \ln(z/\delta_{cw})], \quad (25)$$

where u_z is the measured mean flow velocity at the height z above the bottom.

(3) *Iteration and final estimates*: Results from step (2) are used to compute a new value of C_r as

$$C_r = [1 + 2(u_{*c}/u_{*w})^2 \cos \phi_b + (u_{*c}/u_{*w})^4]^{0.5}, \quad (26)$$

where ϕ_b is the angle between wave and current in the boundary layer. This new C_r is then used to repeat steps (1)–(3) until a convergence of C_r is achieved and the final values of f_{cw} , u_{*c} , u_{*w} , u_{*cw} and δ_{cw} are determined.

The procedures described above are repeated three times, using different roughness heights, to obtain various friction factors and shear velocities. The grain roughness height $k_{bg} = 2.5D$ is first used to obtain the skin-friction factor and shear velocities (u_{*cs} , u_{*ws} and u_{*cws}). Several studies have shown that the friction factor at high-transport stages depends on the thickness of the bedload layer and that the transport-related shear stress due to the combined grain and bedload roughness should be used for predicting ripple geometry and onset

of sand suspension and sheet flow transport (e.g. Wilson, 1988; Wiberg and Harris, 1994; Li and Amos, 1998). Based on the wave tunnel experiment of Sawamoto and Yamashita (1986) and field observations on Sable Island Bank of Li et al. (1997), SEDTRANS96 computes the thickness scale of the bedload layer h_{tm} and the bedload roughness height k_{bt} from

$$h_{tm} = 2.9D(\theta_{cws} - \theta_{cr})^{0.75}, \quad (27)$$

$$k_{bt} = 180h_{tm}, \quad (28)$$

where $\theta_{cws} = \rho u_{*cws}^2 / (\rho_s - \rho)gD$ is the skin-friction combined Shields parameter. The sum of this bedload roughness height and the grain roughness height is used in the second repeat of steps (1)–(3) to obtain the (transport-related) bedload friction factor and bedload shear velocities (u_{*cb} , u_{*wb} and u_{*cwb}). Next, the skin-friction and bedload shear velocities are used in a combined-flow ripple model proposed by Li and Amos (1998; see the following discussion) to obtain ripple height and wavelength which are used to obtain the ripple roughness height $k_{br} = 27.7\eta(\eta/\lambda)$. The ripple roughness height is added to the grain roughness height and bedload roughness height to derive the total roughness height $k_b = k_{bg} + k_{br} + k_{bt}$. Finally, this total roughness height is used in steps (1)–(3) for the third time to derive the total friction factor and total bed shear velocities (u_{*c} , u_{*w} and u_{*cw}) which eventually determine the vertical profiles of velocity and suspended sediment concentration. Based on parameters calculated using the total roughness, apparent bed roughness z_{0c} is obtained as

$$z_{0c} = \delta_{cw} \exp[-(u_{*c}/u_{*cw}) \ln(\delta_{cw}/z_0)], \quad (29)$$

where z_0 now is the total bottom roughness defined as $k_b/30$. The mean velocity 1 m above the sea bed finally is computed from

$$u_{100} = (u_{*c}/\kappa) \ln(1/z_{0c}) \quad \text{for } \delta_{cw} \leq 1 \text{ m}, \quad (30a)$$

$$u_{100} = (u_{*c}/\kappa)(u_{*c}/u_{*cw}) \ln(30 \times 1/z_0) \quad \text{for } \delta_{cw} > 1 \text{ m}. \quad (30b)$$

There are extensive laboratory and field measurements of wave ripples and these have been used to derive several wave-ripple predictors (e.g. Nielsen, 1981; Grant and Madsen, 1982; Boyd et al., 1988; Wiberg and Harris, 1994). In contrast, data on ripples under combined waves and currents are scarce and their prediction is just beginning to be dealt with (Amos et al., 1988; van Rijn et al., 1993; van Rijn and Havinga, 1995; Li et al., 1996; Li and Amos, 1998). Recent field measurements of combined-flow ripples have shown that wave-ripple predictors are not applicable to combined waves and currents (e.g. Osborne and Vincent, 1993; Li et al., 1996). SEDTRANS96 uses the combined-flow ripple predictor proposed by Li and Amos (1998) based

on their field observations of ripples on Scotian Shelf. This ripple predictor separates ripples into five categories: no transport, ripples in weak-transport range, ripples in equilibrium range, ripples in break-off range, and upper-plane bed sheet-flow. For $u_{*cws} < u_{*cr}$, the presence of pre-existing ripples will cause bed shear stress to increase from ripple trough to crest (Wiberg and Nelson, 1992; Li, 1994). This enhanced skin-friction shear velocity at the ripple crest, u_{*cwe} , determines when bedload transport and hence ripple movement will start (Li et al., 1997). The ripple-enhanced shear velocity is calculated according to Nielsen (1986):

$$u_{*cwe} = u_{*cws} / (1 - \pi\eta_p/\lambda_p), \quad (31)$$

where η_p and λ_p are height and wavelength of the pre-existing ripples, respectively. If ripple-enhanced shear velocity u_{*cwe} is less than the critical shear velocity u_{*cr} , there is no sediment transport and the input ripple height and wavelength will be used as the predicted ripple dimension. Otherwise if $u_{*cws} < u_{*cr}$ but $u_{*cwe} > u_{*cr}$, localized sediment transport occurs close to the ripple crest and ripples in this weak-transport range will be predicted from:

$$\eta/D = 19.6(u_{*cws}/u_{*cr}) + 20.9, \quad (32a)$$

$$\eta/\lambda = 0.12. \quad (32b)$$

When the skin-friction combined shear velocity u_{*cws} is greater than the critical shear velocity u_{*cr} but the bedload shear velocity u_{*cwb} is smaller than the ripple break-off shear velocity u_{*bf} , overall bedload transport will occur and ripples will be in the equilibrium range:

$$\eta/D = 27.14(u_{*cwb}/u_{*cr}) + 16.36, \quad (33a)$$

$$\eta/\lambda = 0.15. \quad (33b)$$

for wave-dominant ripples ($u_{*ws}/u_{*cs} \geq 1.25$) and

$$\eta/D = 22.15(u_{*cwb}/u_{*cr}) + 6.38, \quad (34a)$$

$$\eta/\lambda = 0.12 \quad (34b)$$

for current-dominant or combined wave-current ripples ($u_{*ws}/u_{*cs} < 1.25$). The break-off shear velocity u_{*bf} is the critical shear velocity beyond which significant sand by-passing occurs and ripple steepness η/λ starts to decrease from its maximum value obtained in the equilibrium range. This break-off criterion is defined, according to Grant and Madsen (1982), as $u_{*bf} = 1.34S_*^{0.3}u_{*cr}$ in which $S_* = (D/4\nu)[(\rho_s - \rho)gD/\rho]^{0.5}$ is a dimensionless sediment parameter. Under the conditions of $u_{*bf} \leq u_{*cwb} < u_{*up}$, break-off ripples will form and their geometry is predicted from

$$\lambda = 535D, \quad (35a)$$

$$\eta/\lambda = 0.15(u_{*up} - u_{*cwb}) / (u_{*up} - u_{*bf}). \quad (35b)$$

Eq. (35) predicts that ripple wavelength is constant in the break-off range and that the ripple steepness has the maximum value of 0.15 at $u_{*cwb} = u_{*bf}$ and decreases towards 0 as u_{*cwb} approaches the upper-plane bed criterion u_{*up} . Finally, at high transport stages when bedload shear velocity exceeds the critical shear velocity for sheet-flow ($u_{*cwb} \geq u_{*up}$), ripples are completely washed out and upper-plane bed will be predicted (both η and λ will be zero).

3.4. Subroutine TIMING

This subroutine calculates the times during a wave cycle when the respective threshold criteria are exceeded. The main modification in this subroutine is that the shear stresses, instead of shear velocities, are used in the computation of transport times for wave only and combined-flow cases.

For the steady-current case, sediment is always transported in suspended load if current shear velocity u_{*cs} exceeds the critical shear velocity for suspension u_{*crs} . Otherwise, if $u_{*cr} \leq u_{*cs} < u_{*crs}$, then bedload transport always exists. For the pure-wave case, the time of bedload transport in 1/2 wave cycle t_b or that of suspended-load transport t_s can be found by solving the following two equations, respectively:

$$|\tau_{ws} \cos(\omega t_b)| \geq \tau_{cr}, \quad (36a)$$

$$|\tau_{ws} \cos(\omega t_s)| \geq \tau_{crs}, \quad (36b)$$

where τ_{ws} is the skin-friction wave shear stress near the seabed. The value of t_b or t_s is multiplied by 2 to obtain the total transport time in a complete wave cycle.

For the combined-flow case, vectorial addition is used to obtain the instantaneous combined shear stress $\tau_{cws}(t)$ from:

$$\tau_{cws}(t)^2 = [\tau_{ws} \cos(\omega t) + \tau_{cs} \cos(\phi_b)]^2 + [\tau_{cs} \sin(\phi_b)]^2, \quad (37)$$

where ϕ_b is the angle separating the skin-friction current shear stress τ_{cs} from the wave shear stress τ_{ws} . The duration of bedload transport t_b is obtained by solving the following equation:

$$[\tau_{ws} \cos(\omega t_b) + \tau_{cs} \cos(\phi_b)]^2 + [\tau_{cs} \sin(\phi_b)]^2 \geq \tau_{cr}^2. \quad (38)$$

The same procedures are repeated using τ_{crs} to derive the time for suspended-load transport.

3.5. Subroutine TRANSP

The instantaneous sediment transport is integrated through a wave cycle in this subroutine to obtain the time-averaged net sediment transport rate. Five sediment transport formulae are available in

SEDTRANS96: the Engelund-Hansen (1967) total load equation, the Einstein-Brown (Brown, 1950) bedload equation, the Bagnold (1963) total load equation, the Yalin (1963) bedload equation and the method for cohesive sediment transport.

Three key improvements are made in TRANSO subroutine of SEDTRANS96. Firstly, the wave and current shear stresses, instead of shear velocities, are used in the vector addition to obtain the total shear stress for the calculation of sediment transport rates. SEDTRANS92 uses the decomposed wave-parallel and wave-normal components of shear velocity to compute sediment transport rates in these two directions and then vectorially adds these components to obtain the total sediment transport rate. Since sediment transport rate is proportional to the third or higher power of shear velocity, this component approach can significantly under-predict sediment transport rates compared with that calculated directly using the total shear velocity. Thus the second improvement in SEDTRANS96 is that the vectorially added instantaneous combined shear stress is used in the computation of sediment transport rates. The third important change in SEDTRANS96 is that a completely new algorithm for cohesive sediment transport has been proposed based on recent progresses made in this research field (e.g. Amos et al., 1992b, 1996, 1997; Mehta, 1993).

Integration through time is not required for the steady-current case. The symmetry of the linear wave theory also dictates that no net sediment transport will occur for the pure-wave case. For combined waves and current, SEDTRANS96 decomposes the skin-friction current shear stress τ_{cs} into the x (wave-parallel) and y (wave-normal) components based on the angle between waves and current ϕ_b . The x -component of the current shear stress is added to the instantaneous skin-friction wave shear stress $\tau_{ws} \cos(\omega t)$ to obtain the total shear stress in the x direction. This summarized x -component shear stress and the y -component current shear stress are then vectorially added to get the instantaneous combined shear stress $\tau_{cws}(t)$ (see Eq. (37)). Except for the Bagnold equation, this instantaneous combined shear stress is used in all transport formulae to compute the sediment transport rate which is then numerically integrated through the entire wave cycle to obtain the time-average net sediment transport rate (kg/m/s). Each of the chosen sediment transport formulae is briefly described next.

Engelund-Hansen total load equation: The original Engelund-Hansen (1967) equation was based on uni-directional flume experiment data and was derived for dune-covered beds with mean grain sizes larger than 0.15 mm. The modified Engelund-Hansen equation for continental shelf conditions reads

$$q = 0.05 u_{100}^2 \rho^2 u_*^3 / D(\Delta \rho g)^2, \quad (39)$$

where q is the volume rate of sediment transport per unit width of bed, $\Delta\rho$ is equal to $(\rho_s - \rho)$ and u_* is a general-form skin-friction shear velocity.

Einstein–Brown bedload equation: The Einstein–Brown (Brown, 1950) bedload equation was also obtained from flume experiments under unidirectional flow over well-sorted sediment. With shear stress being converted to shear velocity, this equation can be written as:

$$q = 40W_s D(\rho/\Delta\rho g D)^3 u_*^5 |u_*|. \quad (40)$$

The applicable grain size range for the Einstein–Brown equation is 0.3 mm to 29 mm.

Bagnold total load equation: Bagnold (1963) assumed that waves cause sediments to be suspended, but it is the steady currents that cause net sediment transport. Therefore, no integration is required in the Bagnold method. For combined wave–current flows, the maximum (not the instantaneous) skin-friction combined shear stress τ_{cws} is used to compute the net sediment transport rate from

$$q = K\tau_{cws} u_{100}/(\rho_s - \rho)g, \quad (41)$$

where K is the proportionality coefficient described by the empirical equation of Sternberg (1972):

$$K = M \exp[0.7(\tau_{cws} - \tau_{cr})/\tau_{cr}] \quad (42)$$

and the empirical coefficient M has a value of 0.005. The transport direction is assumed to be that of the steady current. For current-only case, the Bagnold's bedload equation modified by Gadd et al. (1978) is used:

$$q = (\beta/\rho_s)(u_{100} - u_{cr})^3, \quad (43)$$

where the critical velocity for the initiation of bedload transport u_{cr} is obtained from $\tau_{cr} = 0.5\rho f_{cs} u_{cr}^2$. Coefficient β (with units of $\text{kg s}^2 \text{m}^{-4}$) is a function of grain size. Gadd et al. analysed flume experiment data and suggested β values of $1.73\text{--}7.22 \times 10^{-3}$ for grain sizes of 0.18–0.45 mm.

Yalin bedload equation: Yalin's (1963) bedload equation states

$$q = 0.635 D u_* [\tau_* - (1/a) \ln(1 + a\tau_*)], \quad (44)$$

where $\tau_* = (\tau_b - \tau_{cr})/\tau_{cr}$ is the normalized excess shear stress and a is equal to $2.45(\rho/\rho_s)^{0.4}(\tau_{cr}/\Delta\rho g D)^{0.5}$. The application of this equation is generally limited to sediment grains of 0.2 mm or coarser.

Cohesive sediment transport: The main changes in cohesive sediment algorithm include the treatment of transport in three states (depositional, erosional and stable states), effects of the variation of critical erosion stress with sediment depth, and the use of a time-difference scheme in numerical integration to compute the final erosion/deposition rates and cohesive sediment concentration.

The key parameters controlling cohesive sediment transport are the applied bed shear stress τ_b , the

critical shear stress for deposition τ_d and the critical shear stress for erosion τ_e . τ_d defines the critical stress value so that deposition will occur only when $\tau_b < \tau_d$. Similarly, τ_e defines the critical stress value so that mud erosion will begin only when $\tau_b \geq \tau_e$. Depending on various relationships among these three parameters, cohesive sediment transport can be separated into three states:

State 1 (Depositional): When the applied bed shear stress τ_b is less than the critical shear stress for deposition τ_d , there is no erosion and only deposition occurs. The mass deposition rate r_d ($\text{kg m}^{-2} \text{s}^{-1}$) is given by

$$r_d = \partial m / \partial t = c_t W_{sc}(1 - \tau_b/\tau_d)(1 - P_s), \quad (45)$$

where $\partial m / \partial t$ is the change in mass m with time t , c_t is the time-dependent mass suspended sediment concentration, W_{sc} is the settling velocity for cohesive sediments, and P_s is a dimensionless probability coefficient of resuspension in the depositional state (ranging from 0 to 0.2 with a default value of 0). Given the small settling velocity of cohesive sediment, uniform concentration through water column can be assumed. So the decrease of sediment concentration with time, c_t , is described by

$$c_t = c_0 - (r_d \Delta t)/h, \quad (46)$$

where c_0 is the initial sediment concentration, h is the flow depth and Δt is the time duration of the deposition process. The deposition duration Δt is divided into 5 min steps and Eqs. (45) and (46) are used to calculate the time-dependent r_d and c_t for each step which are numerically integrated to obtain the final deposition rate and sediment concentration (c) at the end of Δt . If c_t drops below the minimum value of 0.1 mg l^{-1} during the integration, the subroutine will stop and the time when the cohesive sediment concentration reaches this minimum value will be given.

State 2 (Stable state): If the condition of $\tau_d < \tau < \tau_e$ is met, there will be no deposition or erosion and stable state exists. The final sediment concentration c will be equal to the initial concentration c_0 .

State 3 (Erosional): When the applied shear stress τ_b is higher than the critical shear stress for erosion τ_e , sediment erosion will occur and the mass erosion rate r_e ($\text{kg m}^{-2} \text{s}^{-1}$) is defined as

$$r_e = \partial m / \partial t = E_0 \exp[P_e(\tau_b - \tau_e(z))^{0.5}], \quad (47)$$

where E_0 is an empirical coefficient for minimum erosion, P_e is the proportionality coefficient for erosion and $\tau_e(z)$ is the critical shear stress for erosion as a function of erosion depth z_s . According to Amos et al. (1992b), E_0 is equal to 0.000051 and the default value of P_e is 1.62. Recent studies by Amos et al. (1992b, 1996, 1997) have also shown that $\tau_e(z)$ increases as sediment is eroded away and its variation with downcore depth z_s

can be given as

$$\tau_c(z) = \tau_c(0) + A(\rho_b - \rho)gz_s \tan \phi_i \quad (48)$$

in which $\tau_c(0)$ is the critical erosion stress at the sediment surface, A is an empirical coefficient for downcore sediment resistance, ρ_b is the bulk sediment density, and ϕ_i is the internal friction angle of cohesive sediment. In principle, both ρ_b and ϕ_i will change with downcore depth to cause the observed increase of τ_c with z_s . The dependence of ρ_b and ϕ_i on z_s is also site and mud-type specific. An ideal approach would be to specify the downcore variations of ρ_b and ϕ_i for the study site and use Eq. (48) to obtain a downcore profile of $\tau_c(z)$. Given our very limited measurements of ρ_b and ϕ_i with downcore depth, however, it is impossible at the present to do so. Thus for modelling purposes, we have assumed that ρ_b and ϕ_i would be constant with the downcore depth and that an arbitrary value is assigned to the empirical coefficient A to generate a reasonable downcore profile of $\tau_c(z)$. Field and laboratory measurements of $\tau_c(z)$ have shown that $\tau_c(z)$ generally increases 2–4 times as the erosion depth reaches about 4–5 mm (Amos et al., 1996). A conservative value of $A = 0.01$ has been taken in SEDTRANS96 for the prediction of $\tau_c(z)$ to mimic this general trend.

With erosion rate being calculated from Eq. (47), the eroded mass E_m (kg m^{-2}) in the given time interval Δt is computed from

$$E_m = r_e \Delta t. \quad (49)$$

The erosion depth and the new concentration due to this erosion will be

$$z_s = E_m / \rho_b, \quad (50)$$

$$c_t = c_0 + (r_e \Delta t) / h. \quad (51)$$

As for state 1, SEDTRANS96 again divides Δt into 5 min steps and Eqs. (47)–(51) are used to calculate the time-dependent r_e and c_t for each step which are numerically integrated to obtain the final erosion rate and sediment concentration (c) at the end of Δt . If τ_b is found to be smaller than τ_c at a certain erosion depth z_s during the integration, the model will stop and the time when the erosion process ceases will be given.

For all three states described above, the final step is to compute the starting (Q_{s0} , $\text{kg m}^{-1} \text{s}^{-1}$) and ending (Q_s) sediment transport rates of the time duration Δt . Again for these computations, we have assumed a uniform vertical concentration and the mean velocity at 1 m above the sea bed u_{100} is used to represent the depth-averaged mean velocity. The starting sediment transport rate will be

$$Q_{s0} = c_0 h u_{100} \quad (52)$$

and the final sediment transport rate will be

$$Q_s = c h u_{100}. \quad (53)$$

As discussed in detail in Li and Amos (1995), most parameters in the above method must be measured either in situ or in laboratories. The settling velocity for cohesive sediment W_{sc} cannot be predicted by the method used for non-cohesive sediments because of aggregation and flocculation. Graphs of W_{sc} are given in Owen (1970) and Ross (1988). However, field or laboratory measurements are recommended for each particular site to obtain W_{sc} . Different techniques for measuring W_{sc} have been described by Amos and Mosher (1985), McCave and Gross (1991), Kineke et al. (1989), Hill et al. (1994) and Syvitski et al. (1995). There are also no known ways to predict the critical deposition shear stress τ_d , the critical erosion shear stress τ_c , and the down-core variation of ρ_b (and hence τ_c). Measurements have to be done for specific site and mud type since their values depend on mineralogy, degree of consolidation and benthic biological activities. Cited values of τ_d range from 0.3 to 3.2 dyn cm^{-2} , while that of τ_c are from 1.1 to 9.5 dyn cm^{-2} (Amos and Greenberg, 1980; Gust and Morris, 1989; Amos et al., 1996). Physical and rheological properties have also been found to be related to τ_c . For instance, Mimura (1989) shows that τ_c can be calculated from the yield stress τ_y of cohesive sediments as $\tau_c = 0.79 \tau_y^{0.94}$ and Amos et al. (1996) show that τ_c can be related to ρ_b through $\tau_c = 0.0007 \rho_b - 0.47$ (ρ_b in kg m^{-3} to give τ_c in Pascal). It should be pointed out that laboratory measurements inevitably will disturb the original texture, chemistry and biological conditions of the cohesive sediments. In situ measurements using benthic flumes are therefore recommended (Young and Southard, 1978; Amos et al., 1992a).

3.6. Subroutine PROFIL

Another key improvement in SEDTRANS96 is the inclusion of the predictions of the velocity and suspended sediment concentration (ssc) profiles which enable us to calculate the rates of suspended load transport. These computations are dealt with in a new subroutine PROFIL.

For the wave-only case, there is no steady current present and thus no velocity profile will be predicted. Though the suspended-load transport will be zero for this situation due to the absence of current advection, sand can still be resuspended into the water column when wave shear velocity is higher than the critical shear velocity for suspension u_{*crs} . Assuming that sand suspension is mostly concentrated close to the seabed, the mean suspended sediment concentration C_z at the height z is given by the simplified Rouse (1937)

equation

$$C_z = C_0(z/z_0)^{-\alpha}, \quad (54)$$

where C_0 is the reference sediment concentration at the height of bed roughness z_0 and $\alpha = 0.74W_s/\kappa u_{*w}$ is the Rouse suspension parameter in which W_s is the particle settling velocity and u_{*w} is the maximum (not the instantaneous) total wave shear velocity. Based on Smith and McLean (1977), the reference concentration C_0 is calculated from

$$C_0 = \gamma_0 C_b \tau_* / (1 + \tau_*), \quad (55)$$

where $C_b = 0.65$ is the volume concentration of bottom sediment, $\tau_* = (\tau_{ws} - \tau_{cr})/\tau_{cr}$ again is the normalized excess shear stress, with τ_{ws} being the maximum skin-friction wave shear stress, and γ_0 is the empirical sediment resuspension coefficient. The calculation of C_z and C_0 in above two equations does not require integration through the wave cycle. A wide range of γ_0 values has been suggested in the past (Smith and McLean, 1977; Kachel and Smith, 1986; Hill et al., 1988; Drake and Cacchione, 1989). Among other factors such as bed armouring (e.g. Cacchione and Drake, 1990), recent studies by Vincent and Downing (1994) and Li et al. (1996) have shown that sand resuspension is strongly controlled by the development of bedforms. These studies show that the value of γ_0 initially increases with the excess shear stress as ripples grow in the equilibrium range and that when ripples enter the break-off range γ_0 will decrease with the excess shear stress as ripples deteriorate at these high-transport stages. Thus based on the results of Vincent and Downing (1994) and Li et al. (1996), SEDTRANS96 uses the following equations for the predictions of γ_0 in the equilibrium range ($u_{*ws} < u_{*bf}$), in the break-off range ($u_{*bf} \leq u_{*ws} < u_{*up}$) and under the sheet-flow condition ($u_{*ws} \geq u_{*up}$):

$$\gamma_0 = 0.0355 \tau_*^{1.94} \quad \text{for } u_{*ws} < u_{*bf}, \quad (56a)$$

$$\gamma_0 = 0.0206 \tau_*^{-1.93} \quad \text{for } u_{*bf} \leq u_{*ws} < u_{*up}, \quad (56b)$$

$$\gamma_0 = 0.00013 \quad \text{for } u_{*ws} \geq u_{*up}. \quad (56c)$$

For the current-only case, both velocity and ssc profiles will be predicted. The velocity profile is given as

$$u_z = (u_{*c}/\kappa) \ln(z/z_0) \quad (57)$$

and the ssc profile is predicted from Eq. (54) but with $\alpha = 0.74W_s/\kappa u_{*c}$ and u_{*c} is the total current shear velocity. C_0 will be predicted from Eqs. (55) and (56) with τ_{ws} and u_{*ws} being replaced by τ_{cs} and u_{*cs} , respectively. Eq. (57) is valid only when velocity profiles are in logarithmic form. Suspension stratification and flow acceleration/deceleration, among other factors, can cause deviation from this and care must be given when applying Eq. (57) under these conditions.

For the combined wave–current case, the velocity profile will be predicted by Eq. (24). The ssc profiles are predicted using a modified Rouse equation which is proposed by Glenn and Grant (1987) and has been tested with field data by Li et al. (1996):

$$C_z = C_0 (z/z_0)^{-\alpha_1} \quad \text{for } z < \delta_{cw}, \quad (58a)$$

$$C_z = C_{\delta_{cw}} (z/\delta_{cw})^{-\alpha_2} \quad \text{for } z > \delta_{cw}, \quad (58b)$$

where the Rouse suspension parameter within the wave–current boundary layer α_1 is equal to $0.74W_s/\kappa u_{*cw}$ and the Rouse suspension parameter above the wave–current boundary layer α_2 is equal to $0.74W_s/\kappa u_{*c}$. The reference concentration C_0 is calculated from Eqs. (55) and (56) with τ_{ws} and u_{*ws} now being replaced by τ_{cws} and u_{*cwb} , respectively. $C_{\delta_{cw}}$ is the suspended sediment concentration at the top of the wave–current boundary layer δ_{cw} and is given by Eq. (58a) by equating z to δ_{cw} . Again u_{*cw} is the maximum (not instantaneous) total combined shear stress and integration is not necessary in the computation of C_z in Eqs. (58a) and (58b).

After the computation of the velocity and ssc profiles, their product of $u_z C_z$ is numerically integrated over the water depth to obtain the suspended-load transport rate Q_s :

$$Q_s = \int u_z C_z \Delta z,$$

where Δz represents a small increment of height from the seabed. The direction of the suspended-load transport is assumed to be that of the steady current.

3.7. Subroutine BEDFORM

Various bed shear stresses and near-bed velocities (u_{100} for currents, u_b for waves) are used in this subroutine to determine the types of bedforms. The key improvement in SEDTRANS96 is that ripple types under the combined-flow now is predicted based on the recent field study of Li and Amos (1998). For sediments finer than 0.063 mm (silts and clay), there will be no bedform development (although formation of small ripples in silt was observed in a few flume experiments, e.g., Jopling and Forbes, 1979). For gravels ($D > 2$ mm) and coarse to very-coarse sands ($0.5 \text{ mm} < D \leq 2 \text{ mm}$), there is no method available yet for predicting the bedform dimensions and only bedform types will be predicted. For sediments ranging from very-fine sand to medium sand ($0.063 \text{ mm} \leq D \leq 0.5 \text{ mm}$), both bedform type and dimension are predicted.

For sediments coarser than 2 mm, gravel ripples are predicted. For coarse and very coarse sands, current ripples will be predicted if $u_b = 0$ and wave ripples will be defined if $u_{100} = 0$. If neither u_{100} nor u_b is zero, combined-flow ripples are present and the ratio of the

skin-friction wave Shields parameter relative to that of the steady current, θ_{ws}/θ_{cs} , is then used to further define if the ripples are wave dominant ($\theta_{ws}/\theta_{cs} > 1$) or current dominant ($\theta_{ws}/\theta_{cs} \leq 1$). For wave or wave-dominant ripples in this grain size range, u_b is used to predict bedform types according to Amos (1990, Chapter 11, pp. 609–613) as shown in Table 1. For current or current-dominant ripples, u_{100} will be used to predict the bedform types (see Table 1).

For grain sizes ranging from very-fine sand to medium sand, the values of u_b and u_{100} are used to first decide if wave, current or combined-flow ripples are present. For wave ripples or current ripples, u_{*cs} and u_{*ws} are, respectively, compared against various critical shear velocities to determine the following bedform types:

For $u_b = 0$, current ripples

if $u_{*cs} < u_{*cr}$, no transport; input ripple height and wavelength will be used

if $u_{*cs} \geq u_{*up}$, current-induced upper-plane bed

if $u_{*cr} \leq u_{*cs} < u_{*up}$, active current ripples present.

For $u_{100} = 0$, wave ripples

if $u_{*ws} < u_{*cr}$, no transport; input ripple height and wavelength will be used

if $u_{*ws} \geq u_{*up}$, wave-induced upper-plane bed

if $u_{*cr} \leq u_{*ws} < u_{*up}$, active wave ripples present.

If neither u_{100} nor u_b is equal to 0, combined-flow ripples are predicted

For active current ripples, the mean velocity u_{100} is used to further predict sub-types of current ripples according to Amos (1990; see Table 1). The dimensions of active current ripples are predicted based on Yalin (1964) and Allen (1970) as given by Eqs. (18) and (20). The dimensions of active wave ripples are based on Allen (1970) and Boyd et al. (1988) as described by Eqs. (19) and (20).

For combined-flow ripples, ripple-enhanced shear velocity u_{*cwe} , the skin-friction combined shear velocity u_{*cws} and the bedload combined shear velocity u_{*cwb} are compared with various critical shear velocities to determine the following types of bedforms (Li and Amos, 1998):

if $u_{*cwe} < u_{*cr}$, no transport; input ripple height and wavelength will be used

if $u_{*cws} < u_{*cr}$ and $u_{*cwe} \geq u_{*cr}$, weak-transport ripples

if $u_{*cws} \geq u_{*cr}$ and $u_{*cwb} < u_{*bf}$, equilibrium ripples which can be further divided into:

$u_{*ws}/u_{*cs} < 0.75$, current-dominant ripples

$u_{*ws}/u_{*cs} \geq 1.25$, wave-dominant ripples

$0.75 \leq u_{*ws}/u_{*cs} < 1.25$, combined wave/current ripples

if $u_{*bf} \leq u_{*cwb} < u_{*up}$, break-off ripples (wave-dominant)

if $u_{*cwb} \geq u_{*up}$, upper-plane bed under combined flow.

The heights and wavelengths of combined-flow ripples are predicted according to the combined-flow ripple predictor of Li and Amos (1998) which are already given by Eqs. (32)–(35).

Table 1
Near-bed velocities and possible bedform types (modified from Amos, 1990)

Bedform	Bounds	Sand			
		Fine	Medium	Coarse	Very coarse
(1) <i>Current-ripples based on u_{100}</i>					
Lower flat bed	Upper	$< 13 \text{ cm s}^{-1}$	$< 20 \text{ cm s}^{-1}$	$< 25 \text{ cm s}^{-1}$	$< 40 \text{ cm s}^{-1}$
	Lower				
Current ripples	Upper	60 cm s^{-1}	50 cm s^{-1}	35 cm s^{-1}	No ripples
	Lower	13 cm s^{-1}	20 cm s^{-1}	25 cm s^{-1}	
2-D mega-ripples	Upper	No 2-D mega-ripples	60 cm s^{-1}	60 cm s^{-1}	60 cm s^{-1}
	Lower		50 cm s^{-1}	40 cm s^{-1}	40 cm s^{-1}
Sand waves	Upper	No sand waves	100 cm s^{-1}	100 cm s^{-1}	100 cm s^{-1}
	Lower		60 cm s^{-1}	50 cm s^{-1}	40 cm s^{-1}
3-D mega-ripples	Upper	No 3-D mega-ripples	150 cm s^{-1}	150 cm s^{-1}	No 3-D mega-ripples
	Lower		60 cm s^{-1}	60 cm s^{-1}	
Upper-plane bed and sand ribbons	Upper	85 cm s^{-1}	170 cm s^{-1}	240 cm s^{-1}	295 cm s^{-1}
	Lower	60 cm s^{-1}	150 cm s^{-1}	150 cm s^{-1}	100 cm s^{-1}
(2) <i>Wave-ripples based on u_b</i>					
Wave ripples	Upper	70 cm s^{-1}	100 cm s^{-1}	125 cm s^{-1}	200 cm s^{-1}
	Lower	10 cm s^{-1}	13 cm s^{-1}	20 cm s^{-1}	30 cm s^{-1}
Wave induced upper-plane bed	Upper	—	—	—	—
	Lower	70 cm s^{-1}	80 cm s^{-1}	90 cm s^{-1}	100 cm s^{-1}

4. Model calibration

Many sediment transport models have been proposed for combined flow conditions, but there is a lack of good-quality field measurements of the hydrodynamics and seabed responses for the calibration of these models. Under the funding of the Panel on Energy Research and Development and sponsoring by industrial partners (Pan Canadian and Mobil Oil Canada), a research project has been undertaken at the Geological Survey of Canada — Atlantic (GSCA) to study seabed stability and storm sediment transport on Sable Island Bank (SIB), Scotian Shelf (Fig. 1). Various instrument packages have been deployed at different sites in the SIB region and several good-quality data sets have been collected. Some of these data will be used here to test the thresholds of sediment transport modes and the prediction of bedload transport rate in SEDTRANS96. Due to the lack of independent data, the proposed algorithms for suspended sediment concentration profile and cohesive sediment transport will not be tested here.

The first selected data set was collected by the GSCA instrumented tripod RALPH at site 1 of the SIB region (Fig. 1) in 39 m water depth over medium sand sediment ($D = 0.34$ mm) in early winter of 1993 (January 17–February 14). The second data set was collected at site 2 of the region by a S4 wave–current meter and an instrumented tripod similar to RALPH in 57 m water depth over fine sand ($D = 0.20$ mm) in late winter of 1993 (February 27–March 25). The detailed descriptions of field methods, instrumentation and data analyses are given in Li et al. (1997) and Li and Amos (1999b). The wave, current and sediment parameters from these deployments were used in SEDTRANS96 to compute various bed shear stresses and sediment transport rates. The seabed images collected by the tripods were visually analysed to determine the sediment transport modes, ripple height and wavelength, and their migration rate (details in Li et al., 1997, Li and Amos, 1999b). These results were compared against the model-predicted bed shear stresses and sediment transport rates for its calibration.

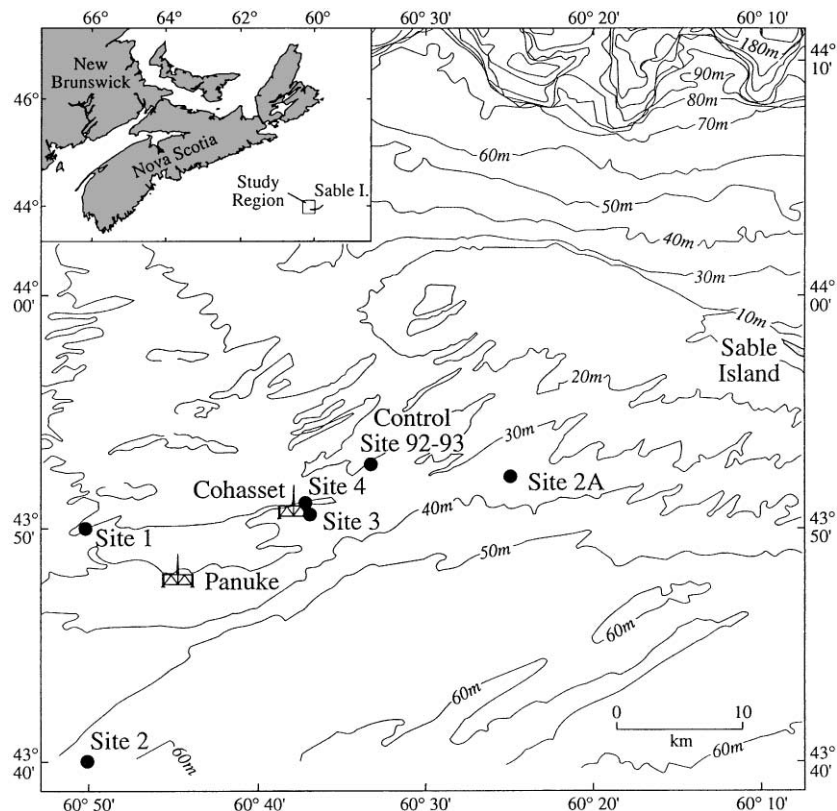


Fig. 1. Location map showing study region on Sable Island Bank, Scotian Shelf, and sites of instrument deployment of GSCA seabed stability and storm sediment transport project. Instrumented tripods and S4 current meters were deployed at site 1 from 15 January to 28 February, 1993; at site 2, from 28 February to 30 April, 1993; at site 2A from 30 April to 16 June, 1993; at site 3 from 24 November, 1993–26 January, 1994 and at site 4 from 7 March to 29 April, 1994. A S4 current meter was also deployed at control site from 15 January to 16 June, 1993.

4.1. Thresholds of sediment transport

The computation of critical shear stresses for various sediment transport modes have been described in the section Subroutine THRESH. In convention the spatially averaged skin-friction shear stress is compared against these critical values to determine the onset of various transport modes. Several studies, however, have shown that when ripples are present or sediment transport is underway, this tends to under-estimate the onset of these transport modes and that the enhanced shear stresses by ripples or bedload transport need to be used for proper predictions of the onset of these transport modes (Kapdasli and Dyer, 1986; Wiberg and Harris, 1994; Li et al., 1997; Li and Amos, 1999b).

Fig. 2A shows the time-series plot of the average skin-friction combined shear velocity u_{*cws} of site 1 data in comparison with the observed transport modes represented by different symbols. The two dashed lines, respectively, indicate the critical shear velocities for bedload (u_{*cr}) and suspended-load (u_{*crs}) transport. The critical shear velocity for sheet-flow u_{*up} is not plotted in Fig. 2A due to the limited range of the vertical axis. Fig. 2A demonstrates that u_{*cws} at the observed initiation of bedload transport, as defined by the boundary between

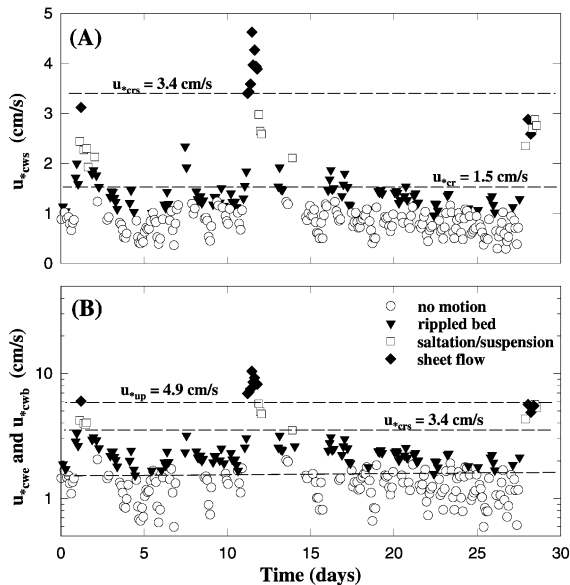


Fig. 2. Time-series plots of combined shear velocities for selected bursts from 1993 site 1 deployment over medium sand: (A) spatially averaged maximum skin-friction combined shear velocity u_{*cws} and (B) ripple-enhanced (u_{*cwe}) or bedload (u_{*cwb}) combined shear velocity. Observed transport modes are indicated by different symbols: open circles, no transport; triangles, bedload transport; squares, sand suspension; and diamonds, sheet-flow transport. Dashed lines, from bottom to top, respectively, represent critical shear velocities for bedload, suspension and sheet-flow transport.

the open circles and triangles, is significantly below the bedload threshold u_{*cr} . Similarly, the observed transition from bedload to suspension transport (defined by the boundary between triangles and squares) and that from suspension to sheet flow (the boundary between squares and diamonds) also occurred at u_{*cws} values much lower than the corresponding critical shear velocities u_{*crs} and u_{*up} . These discrepancies suggest that the direct comparison of the average skin-friction shear velocity with the various critical shear velocities under-estimates the onset of different transport modes. In contrast to Fig. 2A, the ripple-enhanced combined shear velocity u_{*cwe} (for bursts where $u_{*cws} < u_{*cr}$) and the bedload combined shear velocity u_{*cwb} (for bursts where $u_{*cws} \geq u_{*cr}$), computed following the procedures given in the section on subroutine FRICFAC, are plotted in Fig. 2B for the same data set. Now we find that shear velocities at the observed onset of bedload, suspension, and sheet-flow transport are in reasonable agreement with the critical shear velocities for these transport modes. This indicates that the enhanced combined shear velocity at the ripple crest and the combined shear velocity due to bedload transport should be compared against the respective critical shear velocities to determine the initiation of bedload, sand suspension, and sheet-flow transport.

Similar comparisons are also made in Fig. 3 for site 2 data in order to see if the finding obtained from Fig. 2 over medium sand is also valid over fine sand. Here the skin-friction combined shear velocity (u_{*cws} , in open symbols) and the ripple- or bedload-enhanced shear velocities (u_{*cwe} or u_{*cwb} , in solid symbols) during a storm build-up are plotted against time. The observed transport modes are again represented by different symbols and the three dashed lines (from bottom to

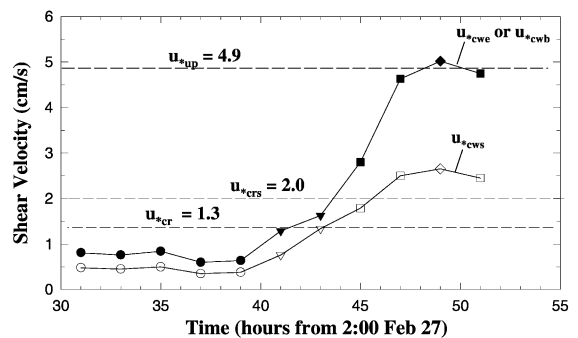


Fig. 3. Time-series plots of spatially-averaged maximum skin-friction (u_{*cws} , in open symbols) and ripple-enhanced or bedload (u_{*cwe} and u_{*cwb} , in solid symbols) combined shear velocities during storm build-up observed during 1993 site 2 deployment over fine-sand sediment. Observed transport modes are again shown by different symbols: circles for no transport, triangles for bedload, squares for suspension, and diamonds for sheet-flow. Three dashed-lines, from bottom to top, respectively represent critical shear velocities for bedload, suspension and sheet-flow transport.

top) indicate the critical shear velocities for bedload, suspension and sheet-flow transport, respectively. Fig. 3 shows that the use of the skin-friction combined shear velocity again causes under-prediction of the onset of various transport modes under combined flow condition. At the observed initiation of bedload transport (hour 40), for instance, u_{*cws} is only about 0.5 cm s^{-1} which is significantly lower than the critical shear velocity of $u_{*cr} = 1.3 \text{ cm s}^{-1}$. Also u_{*cws} is only equal to 2.5 cm s^{-1} when sheet flow was observed and this is much below the established sheet-flow threshold of $u_{*up} = 4.9 \text{ cm s}^{-1}$. When the ripple-enhanced shear velocity u_{*cwe} and bedload shear velocity u_{*cwb} are used, however, much improved agreement is achieved between these critical shear velocities and the observed onset of various transport modes (solid symbols in Fig. 3). This further supports the finding in Fig. 2 for medium sand. Therefore SEDTRANS96 has adopted the use of u_{*cwe} and u_{*cwb} to properly determine the onset of various sediment transport modes.

4.2. Prediction of bedload transport

The four sediment transport formulae for sand used in this model were derived mostly using unidirectional flume data. There have been limited attempts to test the use of these formulae under combined waves and currents by radioactive and fluorescent tracer experiments (Gadd et al., 1978; Heathershaw, 1981; Pattiaratchi and Collins, 1985). In general, these experiments showed that the sediment transport rates predicted using these formulae differed from the measured transport rates by more than one order of magnitude. Based on limited measurements of ripple wavelength and ripple migration rate in a 1982 field experiment on Sable Island Bank (Amos et al., 1988), Li and Amos (1995) calibrated the prediction of bedload transport rates by SEDTRANS92. Though reasonable agreement was found, the testing was for fine sand only. In describing the FRICFAC and TIMING subroutines, we have argued that shear stresses enhanced due to the presence of ripples or bedload transport need to be used to properly predict ripple development and sediment transport time. Conventionally, the spatially averaged instantaneous skin-friction shear stress is used in Eqs. (39)–(44) in the computation of sediment transport rates. If this shear stress increases from ripple trough to crest and the enhanced stress at the ripple crest needs to be used in predicting the onset of bedload transport, one then may ask should this ripple-enhanced instantaneous shear stress also be used for the prediction of sediment transport rates? We are aware that at least one study has suggested the use of this ripple-enhanced shear stress (Wiberg et al., 1994). In this section, we will use site 1 data collected in 1993 over medium sand and the earlier data set collected also on SIB in 1982 over fine sand (see

Li and Amos, 1995, for detailed description) to test the new theories adopted in subroutines FRICFAC and TIMING and to calibrate the predictions of sediment transport rates by SEDTRANS96.

The bedload sediment transport rate can be obtained by considering the volume of sediment involved in the migration of ripples. For a ripple of height η and migration rate R_m , the mean mass transport rate per unit width per unit time will be

$$Q_m = 0.5\rho_b\eta R_m, \quad (59)$$

where ρ_b is the bulk sediment density ($=1.8 \text{ g cm}^{-3}$). The measured ripple heights and migration rates of the 1993 site 1 data and 1982 data under low-to-moderate shear stresses (thus avoiding the effects of sand suspension and upper-plane beds), have been used in Eq. (59) to obtain the measured bedload sediment transport rates Q_m (details of these data sets given in Li and Amos, 1995; Li et al., 1997). For the 1982 data, only ripple wavelengths were measured and the ripple heights were calculated based on Allen (1970) as given by Eq. (20). In the first step, we will use the flow dynamics and ripple migration data collected at site 1 to determine whether the spatially averaged or the ripple-enhanced instantaneous shear stress better predicts sediment transport rates and duration. The Einstein–Brown bedload formula is chosen to do this because this is a bedload method (our measured transport rates based on ripple migration data are predominantly in bedload mode) and it has been tested by limited wave flume data (Madsen and Grant, 1976). The time series of the measured and predicted sediment transport rates, using the spatially averaged instantaneous skin-friction shear stress, are compared in Figs. 4A and B. These plots show that the use of this shear stress severely under-predicts the frequency and duration of sediment transport under site 1 field experiment conditions. This under-prediction is most likely due to the neglect of the shear stress enhancement by ripples (see Fig. 2). The ripple-enhanced instantaneous shear stress $\tau_{cwe} = \rho u_{*cwe}^2$, obtained from Eq. (31), was thus used in the Einstein–Brown formula to predict sediment transport rates for the same set of data and the time series of these predicted transport rates is plotted in Fig. 4C. Comparing Figs. 4A and C indicates that the duration and frequency of sediment transport are reasonably predicted when the ripple-enhanced instantaneous shear stress was used in the TIMING and TRANSP subroutines of SEDTRANS96, though the magnitude seemed to be over-predicted. To further demonstrate this, the ripple-enhanced shear stresses were used in TIMING to determine sediment transport duration and τ_{cws} and τ_{cwe} were then used separately in the Einstein–Brown bedload method to predict sediment transport rates for site 1 data. The measured and predicted sediment transport rates are compared in scatter plots in

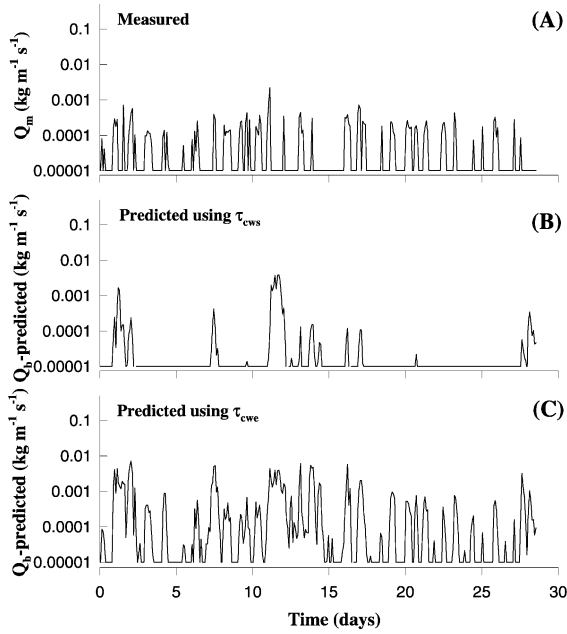


Fig. 4. Time-series plot of (A) measured sediment transport rate Q_m in comparison with predicted sediment transport rates, Q_b -predicted, by Einstein–Brown formula using (B) spatially-averaged skin-friction shear stress τ_{cws} , and (C) ripple-enhanced shear stress, τ_{cwe} . Q_m were calculated using ripple height and migration rate measurements from seabed image analysis.

Figs. 5A and B, respectively. Circles represent the 1993 site 1 data over medium sand and triangles the 1982 data over fine sand. The dashed lines in both figures indicate perfect agreement. Fig. 5 clearly shows that sediment transport rates can be under-predicted by a factor of 5 when the spatially averaged instantaneous skin-friction shear stresses are used. In contrast, the use of the ripple-enhanced instantaneous shear stresses resulted in an over-prediction roughly by a factor of 5, particularly at higher transport rates (Fig. 5B).

When ripples are present, bed shear stress increases from the ripple trough to the crest. It is thus expected that predictions using the maximum value of the enhanced shear stress at the ripple crest will give the highest transport rate across the ripple wavelength and this will not be representative of the mean transport rate averaged across the ripple wavelength. Since sediment transport rate is proportional to the third or higher power of shear velocity, the mean transport rate averaged over the ripple wavelength will be skewed toward the higher values and this may explain the under-prediction by using the spatially averaged skin-friction shear stress. Therefore, an effective shear stress between these two values needs to be found for better prediction of the sediment transport rate. Based on the facts that the ripple-enhancement of shear stress is most effective for ripples in the weak-transport and equilibrium ranges

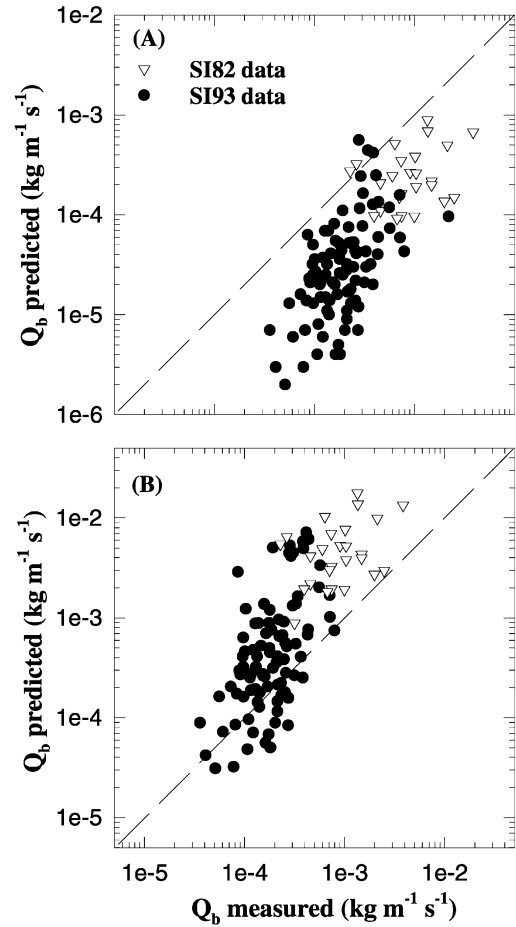


Fig. 5. Scatter plots of measured and predicted sediment transport rates from Einstein–Brown formula using (A) spatially averaged instantaneous skin-friction shear stress and (B) ripple-enhanced instantaneous shear stress. Circles are data from 1993 site 1 deployment over medium sand and triangles are data from 1982 deployment over fine sand. Dashed lines represent perfect agreement.

(in which ripple steepness is at the maximum) and that the effective shear stress should asymptotically approach the average skin-friction shear stress at higher transport stages when the ripple steepness approaches zero, we propose to use the following effective shear stresses, τ'_{cws} , in the TRANSPRO subroutine to predict sediment transport rates at various stages of bedform development:

$$\tau'_{cws} = (\tau_{cr} + \tau_{cwe})/2 \quad \text{for } u_{*cwe} \geq u_{*cr} \text{ and } u_{*cwb} < u_{*bf}, \quad (60a)$$

$$\tau'_{cws} = [1/(2+\sigma)](\sigma\tau_{cr} + \tau_{cws} + \tau_{cwe}) \quad \text{for } u_{*bf} \leq u_{*cwb} < u_{*up}, \quad (60b)$$

$$\tau'_{cws} = \tau_{cws} \quad \text{for } u_{*cwb} \geq u_{*up}, \quad (60c)$$

where $\sigma = (u_{*up} - u_{*cwb}) / (u_{*up} - u_{*bf})$ can be taken as a ripple break-off parameter which indicates how far ripples are into the break-off range and how close they approach the upper-plane bed condition. The physical meaning of Eq. (60) is that in the weak-transport and equilibrium ranges, sediment transport occurs only on a portion of the ripple stoss slope over which the bed shear stress ranges from τ_{cr} to τ_{cwe} . The average of these two values is taken to be the effective bed shear stress at these stages (Eq. (60a)). In the ripple break-off range (Eq. (60b)), all three shear stresses (the critical, the average and the ripple-enhanced) are important when the bedload shear stress just reaches the break-off threshold ($u_{*cwb} = u_{*bf}$ and hence $\sigma = 1$). As u_{*cwb} increases towards u_{*up} , the bed becomes planer and the bed shear stress is higher than τ_{cr} on almost the entire ripple stoss side. Thus the effect of τ_{cr} becomes insignificant (σ approaches 0) and the value of the effective shear stress now mainly depends on the average and ripple-enhanced shear stresses. Finally, when upper-plane bed is reached ((Eq. (60c)), $u_{*cwb} \geq u_{*up}$), there will be no ripple enhancement of the bed shear stress and the effective

shear stress is now equal to the average bed shear stress. The new effective shear stresses given by Eq. (60) have again been used in subroutine TRANSPO for the calculation of sediment transport, and the predicted and measured sediment transport rates are compared in Fig. 6 for the four chosen sediment transport formulae. Compared to Fig. 5, Fig. 6 shows that using the effective shear stresses given by Eq. (60) for different bedform development stages reasonably predicts sediment transport rates for both fine and medium sand and that the error is generally less than a factor of 5 (a large portion of this error is probably due to the uncertainty in the field measurements of ripple height and ripple migration rate). Fig. 6 also shows that the Einstein–Brown bedload method and the Bagnold total load method give the best prediction of sediment transport rates under the combined-flow conditions. Larger scatter exists in the prediction by the Engelund–Hansen total load method, while the Yalin bedload method tends to under-predict sediment transport rates at the low transport stages and slightly over-predicts at higher transport stages.

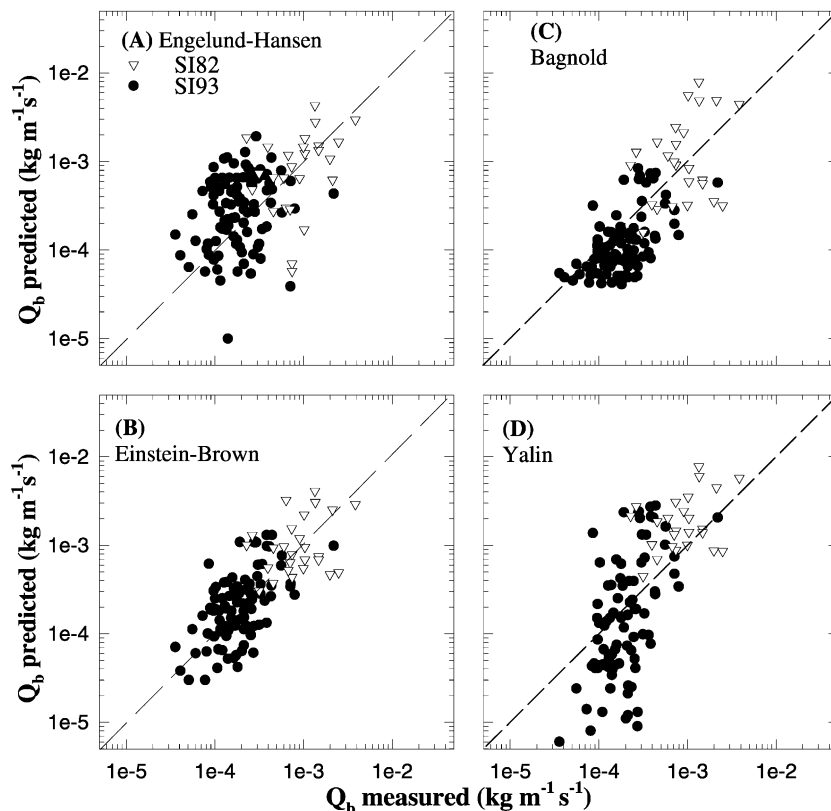


Fig. 6. Scatter plots of measured and predicted sediment transport rates from (A) Engelund–Hansen total-load formula, (B) Einstein–Brown bedload formula, (C) Bagnold total-load and (D) Yalin bedload formula. Proposed effective instantaneous shear stress was used in predictions. Circles are data from 1993 site 1 deployment over medium sand and triangles are data from 1982 deployment over fine sand. Dashed lines represent perfect agreement.

5. Conclusions

The Geological Survey of Canada sediment transport model has been upgraded based on new advances in our understanding of the boundary layer dynamics and sediment transport processes for both cohesive and non-cohesive sediment. The following key improvements are made in SEDTRANS96:

(1) Critical shear stresses for bedload, suspension and sheet-flow transport tested for combined-flow conditions are adopted in SEDTRANS96. It is found that the conventional thresholds for unidirectional flows are applicable under combined waves and currents if the enhanced shear stresses due to the presence of ripples and bedload transport are compared against these criteria.

(2) A combined-flow ripple and bed roughness predictor proposed by Li and Amos (1998) is included in the subroutine FRICFAC so that SEDTRANS96 now can reasonably predict time-dependent bed roughness for combined flows and account for the effects of ripples and bedload transport on bed shear stresses and the profiles of velocity and suspended sediment concentration.

(3) For fine-grained sediments or under storm conditions, suspended-load transport becomes more important. Thus, the modified Rouse (1937) equation is used in this version of the model to predict the vertical profile of sediment suspension and its product with the velocity profile is integrated through depth to obtain the suspended-load sediment flux.

(4) The seabed is often covered by ripples at low-to-moderate transport stages and bed shear stress increases from the ripple trough to the crest under these conditions. Our field data show that using the average skin-friction shear stress or the maximum ripple-enhanced shear stress causes either under- or over-predictions of sediment transport rates. A scheme of effective shear stress as a function of sediment transport and bedform development stages is proposed. The

application of this effective shear stress scheme, as well as the upgraded algorithms for critical shear stress and transport time, has reduced the difference between the measured and predicted sediment transport rates from more than one order of magnitude to generally less than a factor of 5.

(5) Based on new advances in cohesive sediment transport studies, a new cohesive sediment transport algorithm is proposed in SEDTRANS96. Cohesive sediment transport is separated into depositional, stable and erosional states according to the relative values of the applied shear stress, the critical shear stress for deposition and the critical shear stress for erosion. In situ measurements have been used to define a vertical profile of the critical erosion stress $\tau_c(z)$ as a function of down-core depth. This $\tau_c(z)$ profile, the applied shear stress and the erosion/deposition time duration are used in a finite-difference scheme to predict the final erosion/deposition rate and sediment concentration which is multiplied by the mean velocity and water depth to obtain the final sediment transport rate.

Acknowledgements

The authors would like to thank David Heffler, John Zevenhuizen, and Bruce Wile for instrument development and field operation which are critical to the collection of high-quality field data and model calibration. Don Forbes and John Shaw provided critical internal review of the manuscript. Constructive comments from Dr. Peter Flemming and an anonymous journal referee are greatly appreciated. The funding for this work was provided by the Panel on Energy Research and Development (PERD) of the Federal Government of Canada through East Coast Offshore Geotechnics Program 532208. This paper is Geological Survey of Canada Contribution No. 1998216.

Appendix A. A sample run and outputs of IAFSED

```
C:\SED96> menu96
```

```
**** SEDTRANS96 Menu ****
```

1. Run model in interactive mode
2. Run model in batch mode
3. Plot results in Matlab
4. Return to Dos

```
Type the number of your choice and press Enter: 1
```

```
Run SEDTRANS96 in interactive mode
```

```
ENTER FILE NAME IN WHICH OUTPUT WILL BE STORED: TEST1
```

```
IF YOU WISH TO ABORT A RUN, ENTER -99 AS RESPONSE TO ANY OF THE FOLLOWING QUESTIONS
```

ENTER RUN NUMBER (1 - 9999): 1

ENTER WATER DEPTH (m): 23

ENTER CURRENT SPEED, DIRECTION AND HEIGHT ABOVE SEABED (m/s, degrees, m): 0.3 10 0.5

ENTER WAVE HEIGHT, PERIOD AND DIRECTION (m, seconds, degrees): 1 10 20

ENTER GRAIN SIZE, RIPPLE HEIGHT AND LENGTH (m): 0.00023 0.01 0.1

ENTER BED SLOPE (degrees): 5

CHOOSE BETWEEN:

1 - ENGELUND-HANSEN (1967) TOTAL LOAD EQUATION

2 - EINSTEIN-BROWN (1950) BEDLOAD EQUATION

3 - BAGNOLD (1963) TOTAL LOAD EQUATION

4 - YALIN (1963) BEDLOAD EQUATION

5 - COHESIVE SEDIMENT TRANSPORT EQUATION

ENTER 1,2,3,4 OR 5: 2

WARNING

EINSTEIN-BROWN FORMULA IS BASED ON LABORATORY EXPERIMENTS USING SEDIMENTS WITH GRAIN SIZES OF 0.3 TO 28.6 MM

CHECK INPUT DATA FOR RUN #1

SELECT NEW VALUE FOR SEDIMENT GRAIN SIZE? (ENTER Y/N): N

File TEST1:

SEDTRANS96: A SEDIMENT TRANSPORT MODEL
FOR CONTINENTAL SHELF CONDITIONS

GEOLOGICAL SURVEY OF CANADA (ATLANTIC)

CREATED: SEPTEMBER, 1992

LAST UPDATED: DECEMBER, 1996

THE USER SHOULD BE FAMILIAR WITH THE EQUATIONS USED AND THEIR LIMITATIONS

ALL DIMENSIONAL VARIABLES ARE IN SI UNITS

RUN NUMBER 1

INPUT DATA:

WATER DEPTH = 23.00 M

CURRENT SPEED = 0.30 M/SEC

CURRENT DIRECTION = 10.00 DEGREES NORTH

HEIGHT ABOVE BED = 0.50 M

WAVE HEIGHT = 1.00 M

WAVE PERIOD = 10.00 SEC

WAVE DIRECTION = 20.00 DEGREES NORTH

FLUID DENSITY = 1025.0 KG/M³

SEDIMENT DENSITY = 2650.0 KG/M³

SEDIMENT GRAIN SIZE = 0.000230 M

FRACTION OF SEABED MATERIAL = 1.00

RIPPLE HEIGHT = 0.0100 M

RIPPLE LENGTH = 0.1000 M

RESULTS:

MAX. WAVE-INDUCED BOTTOM HORIZONTAL PARTICLE
VELOCITY, FROM LINEAR WAVE THEORY = 0.224 M/SEC

MAX. WAVE-INDUCED BOTTOM HORIZONTAL PARTICLE
DISPLACEMENT, FROM LINEAR WAVE THEORY = 0.357 M

WAVELENGTH, FROM LWT DISPERSION EQUATION = 127.03 M

BOTTOM FRICTION FACTOR
 (GRANT AND MADSEN, 1986) = 0.0098
 CURRENT SPEED 1 M. ABOVE SEABED = 0.35 M/SEC
 CURRENT SPEED TO BE USED IN BOTTOM STRESS CALCULATIONS = 0.16 M/SEC
 ANGLE BETWEEN WAVE AND CURRENT DIRECTIONS WITHIN WAVE BOUNDARY LAYER = 10.00 DEGREES
 NOTE: THIS APPLIES TO MIXED FLOW CONDITIONS ONLY
 CRITICAL SHEAR VELOCITY FOR INITIATION OF BEDLOAD TRANSPORT = 0.0134 M/SEC
 CRITICAL SHEAR VELOCITY FOR INITIATION OF SUSPENDED LOAD TRANSPORT = 0.0200 M/SEC
 TIME, AFTER PASSAGE OF WAVE CREST, AT WHICH SUSPENDED LOAD TRANSPORT CEASES = 2.16 SEC
 TIME, AFTER PASSAGE OF WAVE CREST, AT WHICH BEDLOAD TRANSPORT CEASES = 2.94 SEC
 TIME, AFTER PASSAGE OF WAVE CREST, AT WHICH SUSPENDED LOAD TRANSPORT RECOMMENCES = 0.00 SEC
 TIME, AFTER PASSAGE OF WAVE CREST, AT WHICH BEDLOAD TRANSPORT RECOMMENCES = 0.00 SEC
 PERCENT OF TIME IN ONLY BEDLOAD TRANSPORT PHASE = 15.68
 PERCENT OF TIME IN SUSPENDED LOAD TRANSPORT PHASE = 43.14
 DIRECTION OF NET SEDIMENT TRANSPORT = 15.3 DEGREES TRUE NORTH
 TIME-AVERAGED NET SEDIMENT TRANSPORT = 0.3752E-06 M³/SEC/M
 0.000994 KG/SEC/M
 EINSTEIN-BROWN (1950) BEDLOAD EQUATION
 FRICTION FACTOR FROM GRANT & MADSEN (1986)
 (FOR WAVE-DOMINATED FLOWS)
 EXPECTED BEDFORMS ARE (AMOS, 1990; LI AND AMOS, 1998):
 FINE OR VERY FINE SAND (WENTWORTH SCALE)
 COMBINED-FLOW BEDFORMS PREDICTED BASED ON SIB DATA OF LI AND AMOS (1998)
 BREAK-OFF RIPPLES
 WAVE-CURRENT RIPPLES
 RIPPLE HEIGHT = 0.003 M
 RIPPLE LENGTH = 0.122 M

ENTER 1 TO DO ANOTHER RUN, 0 TO STOP: 0

File SEDOUTI1

bt#	u_b	A_b	f_{cws}	δ_{cw}	z_0	z_{0c}	η	λ
1	0.2245	0.3573	0.0098	0.0613	0.0010	0.0059	0.0027	0.1219

File SEDOUTI2

bt#	u_{*cs}	u_{*ws}	u_{*cws}	u_{*c}	u_{*w}	u_{*cw}	Q_b	Q_s	Q_{b-dir}
1	0.0162	0.0201	0.0258	0.0271	0.0399	0.0481	0.000994	0.007549	5.3

File PROFILE.DAT

bt#	1		
HEIGHT,M		VEL. M/S	CONC. KG/M ³
0.010000		0.088861	1.476115
0.020000		0.115257	0.757329
0.030000		0.130698	0.512556
0.050000		0.150151	0.313432

0.070000	0.166899	0.205233
0.100000	0.191045	0.111460
0.200000	0.237969	0.034031
0.300000	0.265418	0.017001
0.500000	0.300000	0.007092
0.700000	0.322778	0.003987
1.000000	0.346924	0.002165
2.000000	0.393849	0.000661

Appendix B. Input and output files for running BCHSED**File INDATA:**

bt#	h	u _z	z _r	C _{dir}	H _s	T	W _{dir}	D	η	λ	β	F	ρ _s	ρ	I	c ₀	τ _c	τ _d	t	W _{sc}
1	23	0.14	1.0	10	0.85	8.0	20	0.00023	0.01	0.1	0	1	2650	1025	2	0	0	0	0	0
2	23	0.15	1.0	20	0.85	8.0	20	0.00023	0.01	0.1	0	1	2650	1025	2	0	0	0	0	0
3	23	0.20	1.0	30	0.90	8.5	20	0.00023	0.01	0.1	0	1	2650	1025	2	0	0	0	0	0
4	23	0.22	1.0	40	1.00	8.5	20	0.00023	0.01	0.1	0	1	2650	1025	2	0	0	0	0	0
5	23	0.25	1.0	50	1.20	9.0	20	0.00023	0.01	0.1	0	1	2650	1025	2	1	0	0	0	0

File SEDOUT1.DAT

bt#	u _b	A _b	f _{cws}	δ _{cw}	z ₀	z _{0c}	η	λ
1	0.1443	0.1837	0.0127	0.0373	0.0019	0.0131	0.0124	0.0828
2	0.1443	0.1837	0.0126	0.0380	0.0020	0.0127	0.0126	0.0838
3	0.1679	0.2272	0.0116	0.0461	0.0020	0.0121	0.0144	0.1219
4	0.1866	0.2524	0.0113	0.0469	0.0016	0.0103	0.0117	0.1219
5	0.2413	0.3457	0.0104	0.0528	0.0010	0.0086	0.0052	0.1219

File SEDOUT2.DAT

bt#	u* _{cs}	u* _{ws}	u* _{cws}	u* _c	u* _w	u* _{cw}	Q _b	Q _s	Q _{b-dir}
1	0.0075	0.0132	0.0152	0.0129	0.0343	0.0366	0.000382	0.006537	15.3
2	0.0079	0.0133	0.0155	0.0137	0.0347	0.0373	0.000447	0.006776	20.0
3	0.0103	0.0154	0.0185	0.0181	0.0386	0.0426	0.000384	0.007760	24.6
4	0.0113	0.0168	0.0201	0.0192	0.0391	0.0434	0.000448	0.005882	29.2
5	0.0132	0.0204	0.0239	0.0210	0.0415	0.0460	0.000713	0.003828	33.4

File PROFILE

BT#	1	
HEIGHT,M	VEL.M/S	CONC. KG/M ³
0.010000	0.018865	13.815163
0.020000	0.026753	5.747019
0.030000	0.031367	3.440508
0.050000	0.043299	0.912789
0.070000	0.054160	0.272793
0.100000	0.065673	0.075823
0.200000	0.088048	0.006298
0.300000	0.101136	0.001469
0.500000	0.117625	0.000235
0.700000	0.128487	0.000070
1.000000	0.140000	0.000020
2.000000	0.162375	0.000002

BT#	2	
HEIGHT,M	VEL.M/S	CONC. KG/M ³
0.010000	0.020702	12.444311
0.020000	0.029483	5.257009
0.030000	0.034620	3.175609

0.050000	0.047059	0.936918
0.070000	0.058621	0.301271
0.100000	0.070878	0.090496
0.200000	0.094696	0.008741
0.300000	0.108629	0.002227
0.500000	0.126182	0.000398
0.700000	0.137744	0.000128
1.000000	0.150000	0.000038
2.000000	0.173818	0.000004

BT# 3

HEIGHT,M	VEL.M/S	CONC. KG/M ³
0.010000	0.031198	6.669628
0.020000	0.044553	3.136289
0.030000	0.052365	2.017123
0.050000	0.064332	1.025931
0.070000	0.079570	0.433750
0.100000	0.095723	0.174145
0.200000	0.127113	0.029560
0.300000	0.145476	0.010475
0.500000	0.168609	0.002835
0.700000	0.183847	0.001199
1.000000	0.200000	0.000481
2.000000	0.231391	0.000082

BT# 4

HEIGHT,M	VEL.M/S	CONC. KG/M ³
0.010000	0.039794	3.903410
0.020000	0.054598	1.860415
0.030000	0.063257	1.206005
0.050000	0.075870	0.641451
0.070000	0.092058	0.285257
0.100000	0.109218	0.120831
0.200000	0.142567	0.022761
0.300000	0.162075	0.008572
0.500000	0.186651	0.002505
0.700000	0.202840	0.001114
1.000000	0.220000	0.000472
2.000000	0.253349	0.000089

BT# 5

HEIGHT,M	VEL.M/S	CONC. KG/M ³
0.010000	0.055530	1.649636
0.020000	0.072155	0.821021
0.030000	0.081880	0.545871
0.050000	0.094132	0.326411
0.070000	0.110276	0.165760
0.100000	0.129017	0.075488
0.200000	0.165436	0.016369
0.300000	0.186740	0.006694
0.500000	0.213580	0.002170
0.700000	0.231259	0.001033
1.000000	0.250000	0.000471
2.000000	0.286420	0.000102

References

- Ackers, P., White, W.R., 1973. Sediment transport: new approach and analysis. *Journal of Hydraulics Division*, Proceedings of ASCE 99 (HY11), 2041–2060.
- Allen, J.R.L., 1970. *Physical Processes and Sedimentation*. Unwin University Books, London, 248pp.
- Amos, C.L., 1990. Modern sedimentary processes. In: *Geology of the Continental Margin of Eastern Canada*, Geological Survey of Canada, *Geology of Canada* 2.
- Amos, C.L., Bowen, A.J., Huntley, D.A., Lewis, C.F.M., 1988. Ripple generation under the combined influences of waves and currents on the Canadian continental shelf. *Continental Shelf Research* 8 (10), 1129–1153.
- Amos, C.L., Brylinsky, M., Lee, S., O'Brien, D., 1996. Littoral mudflat stability monitoring the Humber estuary, S. Yorkshire, England LISPUC, April, 1995. Geological Survey of Canada Open File Report 3214. 46pp.
- Amos, C.L., Daborn, G.R., Christian, H.A., Atkinson, A., Robertson, A., 1992b. In situ erosion measurements on fine-grained sediments from the Bay of Fundy. *Marine Geology* 108, 175–196.
- Amos, C.L., Feeney, T., Sutherland, T.F., Luternauer, J.L., 1997. The stability of fine-grained sediments from the Fraser River delta. *Estuarine, Coastal and Shelf Science* 45, 507–524.
- Amos, C.L., Grant, J., Daborn, G.R., Black, K., 1992a. Sea carousel — a benthic, annular flume. *Estuarine, Coastal and Shelf Science* 34 (6), 557–577.
- Amos, C.L., Greenberg, D.A., 1980. The simulation of suspended particulate matter in the Minas Basin, Bay of Fundy — a region of potential tidal power development. Proceedings Canadian Coastal Conference, Burlington, Ontario, pp. 2–20.
- Amos, C.L., Mosher, D.C., 1985. Erosion and deposition of fine-grained sediments from the Bay of Fundy. *Sedimentology* 32 (6), 815–832.
- Anderson, C., 1995. A two-dimensional, time-dependent sediment transport model of Sable Island Bank using SEDTRANS92. Challenger Oceanography Consultant Report, GSC Open File Report 2359.
- Bagnold, R.A., 1963. Mechanics of marine sedimentation. In: Hill, M.N. (Ed.), *The Sea*, Vol. 3. Wiley-Interscience, New York, pp. 507–527.
- Bagnold, R.A., 1966. An approach to the sediment transport problem from general physics. US Geological Survey Professional Paper, 4421, 37pp.
- Boyd, R., Forbes, D.L., Heffler, D.E., 1988. Time-sequence observations of wave-formed sand ripples on an ocean shoreface. *Sedimentology* 35, 449–464.
- Brown, C.B., 1950. In: Rouse, H. (Ed.), *Engineering Hydraulics*. Wiley, New York, 1039pp.
- Cacchione, D.A., Drake, D.E., 1990. Shelf sediment transport: an overview with applications to the Northern California continental shelf. In: Le Mehaute, B., Hanes, D.M. (Eds.), *The Sea*, Vol. 9. Wiley-Interscience, New York, pp. 729–773.
- Davidson, S., Amos, C.L., 1985. A re-evaluation of SED1D and SED2D: sediment transport models for the continental shelf. Geological Survey of Canada Open File Report 1705, Section 2, 54pp.
- Dick, J.E., Erdman, M.R., Hanes, D.M., 1994. Suspended sand concentration events due to shoaled waves over a flat bed. *Marine Geology* 119, 67–73.
- Dingler, J.R., Inman, D.L., 1976. Wave-formed ripples in nearshore sands. Proceedings of the 15th Coastal Engineering Conference, ASCE, New York, pp. 2109–2126.
- Drake, D.E., Cacchione, D.A., 1989. Estimates of the suspended sediment reference concentration (C_a) and resuspension coefficient (γ) from near-bed observations on the California shelf. *Continental Shelf Research* 9, 51–64.
- Engelund, F., Hansen, E., 1967. A monograph on sediment transport in alluvial streams. Teknisk Vorlag, Copenhagen, Denmark, 62pp.
- Forbes, D.L., Boyd, R., 1987. Gravel ripples on the inner Scotian Shelf. *Journal of Sedimentary Petrology* 57, 46–54.
- Gadd, P.E., Lavelle, J.W., Swift, D.J.P., 1978. Estimates of sand transport on the New York shelf using near-bottom current-meter observations. *Journal of Sedimentary Petrology* 48, 239–252.
- Gibbs, R.J., Mathews, M.D., Link, D.A., 1971. The relationship between sphere size and settling velocity. *Journal of Sedimentary Petrology* 41, 7–18.
- Glenn, S.M., Grant, W.D., 1987. A suspended sediment stratification correction for combined wave and current flows. *Journal of Geophysical Research* 92, 8244–8264.
- Grant, W.D., Madsen, O.S., 1979. Combined wave and current interaction with a rough bottom. *Journal of Geophysical Research* 84, 1797–1808.
- Grant, W.D., Madsen, O.S., 1982. Movable bed roughness in unsteady oscillatory flow. *Journal of Geophysical Research* 87, 469–481.
- Grant, W.D., Madsen, O.S., 1986. The continental shelf bottom boundary layer. *Annual Review of Fluid Mechanics* 18, 265–305.
- Gust, G., Morris, M.J., 1989. Erosion thresholds and entrainment rates of undisturbed in-situ sediments. *Journal of Coastal Research* (Special Issue) 5, 87–100.
- Hay, A.E., Bowen, A.J., 1993. Spatially correlated depth changes in the nearshore zone during autumn storms. *Journal of Geophysical Research* 98, 12387–12404.
- Heathershaw, A.D., 1981. Comparisons of measured and predicted sediment transport rates in tidal currents. *Marine Geology* 42, 75–104.
- Hill, P.S., Nowell, A.R.M., Jumars, P.A., 1988. Flume evaluation of the relationship between suspended sediment concentration and excess boundary shear stress. *Journal of Geophysical Research* 93, 12499–12509.
- Hill, P.S., Sherwood, C.R., Sternberg, R.W., Nowell, A.R.M., 1994. In situ measurements of particle settling velocity on the northern California continental shelf. *Continental Shelf Research* 14, 1123–1137.
- Jonsson, I.G., 1966. Wave boundary layers and friction factors. Proceedings of the 10th International Conference on Coastal Engineering, Tokyo, pp. 127–148.
- Jopling, A.V., Forbes, D.L., 1979. Flume study of silt transportation and deposition. *Geografiska Annaler* 61A, 67–85.
- Kachel, N., Smith, J.D., 1986. Geological impact of sediment transporting events on the Washington continental shelf. In: Knight, R.J., McLean, J.R. (Eds.), *Shelf Sands and*

- Sandstones. Canadian Society of Petroleum Geologists, Memoir II. Rolands Printing, Calgary, Canada. pp. 145–162.
- Kapdasli, M.S., Dyer, K.R., 1986. Threshold conditions for sand movement on a rippled bed. *Geo-Marine Letters* 6, 161–164.
- Kineke, G.C., Sternberg, R.W., Johnson, R., 1989. A new instrument for measuring settling velocities in situ. *Marine Geology* 90, 149–158.
- Komar, P.D., Miller, M.C., 1975. The initiation of oscillatory ripple marks and the development of plane-bed at high shear stresses under waves. *Journal of Sedimentary Petrology* 45, 697–703.
- Li, M.Z., 1994. Direct skin friction measurements and stress partitioning over movable sand ripples. *Journal of Geophysical Research* 99, 791–799.
- Li, M.Z., Amos, C.L., 1995. SEDTRANS92: A sediment transport model for continental shelves. *Computers & Geosciences* 21 (4), 533–554.
- Li, M.Z., Amos, C.L., 1997. SEDTRANS96: Upgrade and calibration of the GSC sediment transport model. Geological Survey of Canada Atlantic Open File Report 3512, 140pp.
- Li, M.Z., Amos, C.L., 1998. Predicting ripple geometry and bed roughness under combined waves and currents in a continental shelf environment. *Continental Shelf Research* 18 (9), 941–970.
- Li, M.Z., Amos, C.L., 1999a. Sheet flow and large wave ripples under combined waves and currents: their field observation, model prediction and effects on boundary layer dynamics. *Continental Shelf Research* 19, 637–663.
- Li, M.Z., Amos, C.L., 1999b. Field observations of bedforms and sediment transport thresholds of fine sand under combined waves and currents. *Marine Geology* 158, 147–160.
- Li, M.Z., Amos, C.L., Heffler, D.E., 1997. Boundary layer dynamics and sediment transport under storm and non-storm conditions on the Scotian shelf. *Marine Geology* 141, 157–181.
- Li, M.Z., Wright, L.D., Amos, C.L., 1996. Predicting ripple roughness and sand resuspension under combined flows in a shoreface environment. *Marine Geology* 130, 139–161.
- Maa, J.P.-Y., Wright, L.D., Lee, C.-H., Shannon, T.W., 1993. VIMS sea carousel: a field instrument for studying sediment transport. *Marine Geology* 115, 271–287.
- Madsen, O.S., Grant, W.D., 1976. Sediment transport in the coastal environment. MIT, Department of Civil Engineering, Report No. 209, 105pp.
- Madsen, O.S., Wright, L.D., Boon, J.D., Chisholm, T.A., 1993. Wind stress, bed roughness and sediment suspension on the inner shelf during an extreme storm event. *Continental Shelf Research* 13, 1303–1324.
- Manohar, M., 1955. Mechanics of bottom sediment movement due to wave action. U.S. Army Corps Engineers, Beach Erosion Board, Technical Memorandum No. 75, Washington, DC, 121pp.
- Martec Ltd., 1984. SED1D: A sediment transport model for the continental shelf. Unpublished report submitted to the Geological Survey of Canada, DSS Contract IOSC, 23420-3-M753, 63pp.
- Martec Ltd., 1987. Upgrading of AGC sediment transport model. Geological Survey of Canada Open File Report 1705, Section 10, 14pp.
- McCave, I.N., Gross, T.F., 1991. In-situ measurements of particle settling velocity in the deep sea. *Marine Geology* 99, 403–411.
- Mehta, A.J. (Ed.), 1993. Nearshore and Estuarine Cohesive Sediment transport, Coastal and Estuarine Studies, Vol. 42. American Geophysical Union, Washington, DC, 592pp.
- Miche, R., 1944. Mouvements ondulatoires des mers en profondeur constante ou décroissante. *Annales des Ponts et Chausses* 25–78.
- Miller, M.C., McCave, I.N., Komar, P.D., 1977. Threshold of sediment motion under unidirectional currents. *Sedimentology* 24, 507–527.
- Mimura, N., 1989. Recent Japanese studies on cohesive sediment transport. *Journal of Coastal Research (Special Issue)* 5, 101–115.
- Nielsen, P., 1979. Some basic concepts of wave sediment transport. Institute for Hydrodynamics and Hydraulic Engineering, Technical University of Denmark, Serie Paper 20, 160pp.
- Nielsen, P., 1981. Dynamics and geometry of wave generated ripples. *Journal of Geophysical Research* 86, 6467–6472.
- Nielsen, P., 1986. Suspended sediment concentrations under waves. *Coastal Engineering* 10, 23–31.
- Osborne, P.D., Vincent, C.E., 1993. Dynamics of large and small scale bedforms on a macrotidal shoreface under shoaling and breaking waves. *Marine Geology* 115, 207–226.
- Owen, M.W., 1970. A detailed study of settling velocities of an estuary mud. Hydraulics Research Station, Report INT 78, 25pp.
- Pattiaratchi, C.B., Collins, M.B., 1985. Sand transport under the combined influence of waves and tidal currents: An assessment of available formulae. *Marine Geology* 67, 83–100.
- Ross, M.A., 1988. Vertical structure of estuarine fine sediment suspensions, Ph.D. Dissertation, University of Florida, Gainesville.
- Rouse, H., 1937. Modern conceptions of the mechanics of turbulence. *Transactions of the American Society of Civil Engineers* 102.
- Sawamoto, M., Yamashita, T., 1986. Sediment transport rate due to wave action. *Journal of Hydroscience and Hydraulic Engineering* 4, 1–15.
- Smith, J.D., 1977. Modelling of sediment transport on continental shelves. In: Goldberg, E.D., McCave, I.N., O'Brien, J.J., Steele, J.H. (Eds.), *The Sea*, Vol. 6. Wiley-Interscience, New York, pp. 539–576.
- Smith, J.D., McLean, S.R., 1977. Spatially averaged flow over a wavy surface. *Journal of Geophysical Research* 82, 1735–1746.
- Soulsby, R.L., 1983. The bottom boundary layer of shelf seas. In: Johns, B. (Ed.), *Physical Oceanography of Coastal and Shelf Seas*. Elsevier Science Publishers, Amsterdam, pp. 189–266.
- Sternberg, R.W., 1972. Predicting initial motion and bedload transport of sediment particles in the shallow marine environment. In: Swift, D.J.P., Duane, D.B., Pilkey, O.H. (Eds.), *Shelf Sediment Transport, Process and Pattern*, Dowden, Hutchinson & Ross, Inc., pp. 61–83.
- Syvitski, J.P.M., Asprey, K.W., LeBlanc, K.W.G., 1995. In-situ characteristics of particles settling within a deep-water estuary. *Deep-Sea Research II* 42, 223–256.

- van Rijn, L.C., Havinga, F.J., 1995. Transport of fine sands by currents and waves. II. *Journal of Waterway Port, Coastal and Ocean Engineering*, American Society of Civil Engineers 121 (2), 123–133.
- van Rijn, L.C., Nieuwjaar, M.W.C., Van der Kaay, T., Nap, E., van Kampen, A., 1993. Transport of fine sands by currents and waves. *Journal of Waterway Port, Coastal and Ocean Engineering*, American Society of Civil Engineers 119 (2), 123–143.
- Vincent, C.E., Downing, A., 1994. Variability of suspended sand concentrations, transport and eddy diffusivity under non-breaking waves on the shoreface. *Continental Shelf Research* 14, 223–250.
- Wiberg, P.L., Drake, D.E., Cacchione, D.A., 1994. Sediment resuspension and bed armouring during high bottom stress events on the northern California inner continental shelf: measurements and predictions. *Continental Shelf Research* 14 (10/11), 1191–1219.
- Wiberg, P.L., Harris, C.K., 1994. Ripple geometry in wave-dominated environments. *Journal of Geophysical Research* 99, 775–789.
- Wiberg, P.L., Nelson, J.M., 1992. Unidirectional flow over asymmetric and symmetric ripples. *Journal of Geophysical Research* 97, 12745–12761.
- Wilson, K.C., 1988. Mobile-bed friction at high shear stress. *Journal of Hydraulic Engineering* American Society of Civil Engineers 115 (6), 825–830.
- Wright, L.D., 1989. Benthic boundary layers of estuarine and coastal environments. *Reviews in Aquatic Science* 1, 75–95.
- Wright, L.D., 1993. Micromorphodynamics of the inner continental shelf: a Middle Atlantic Bight case study. *Journal of Coastal Research* (Special Issue) 15, 93–124.
- Wright, L.D., Xu, J.P., Madsen, O.S., 1994. Across-shelf benthic transports on the inner shelf of the Middle Atlantic Bight during the “Halloween storm” of 1991. *Marine Geology* 118, 61–77.
- Xu, J.P., Wright, L.D., Boon, J.D., 1994. Estimation of bottom stress and roughness in Lower Chesapeake Bay by the inertial dissipation method. *Journal of Coastal Research* 10, 329–338.
- Yalin, M.S., 1963. An expression for bedload transportation. *Journal of Hydraulics Division, Proceedings ASCE* 89 (HY3), 221–250.
- Yalin, M.S., 1964. Geometrical properties of sand waves. *Journal of Hydraulics Division, Proceedings ASCE* 90 (HY5), 105–119.
- Young, R.N., Southard, J.B., 1978. Erosion of fine-grained marine sediments: sea-floor and laboratory experiments. *Geological Society America Bulletin* 89, 663–672.